npj | flexible electronics

Review

Published in partnership with Nanjing Tech University

https://doi.org/10.1038/s41528-026-00545-5

Materials, processing, and structural strategies for encapsulation in stretchable and flexible optoelectronics

Hyeonji Yoo[1,6], So-Hyeon Lee[2,6], Ji-Youn Kwak[1], Su-Min Kim[1], Hoe-Yeon Jeong[1], Ji-Hyeon Jo[1], Younghoon Kim[3], Youngju Sim[1], Dong-Hyeon Kim[3], Jiheon Jeon[1], Sukwon Hong[1], Soo-Jeong Kim[3], Gyeong-Seok Hwang[4], Ji-Woo Gu[2,5], Han-Hee Cho[1,2], Seung-Kyun Kang[5] & Ju-Young Kim[1,2,3] ✉

Deformable optoelectronic devices are emerging as critical technologies for wearable healthcare systems and next-generation display and energy harvesting platforms. Their practical deployment, however, remains limited by accelerated degradation under ambient conditions. Penetration of water vapor and oxygen accelerates the failure of moisture-sensitive layers, making encapsulation a key determinant of operational lifetime. A fundamental trade-off exists between barrier performance and mechanical stretchability: organic materials offer high compliance but poor moisture resistance, whereas inorganic barriers provide excellent impermeability but suffer from brittleness. Addressing these competing requirements demands an integrated approach that considers material selection and fabrication methodology. This review highlights recent advances in stretchable encapsulation technologies, encompassing organic, inorganic, and hybrid materials, and outlines the core requirements for practical operation: high impermeability, mechanical compliance, and optical transparency. By correlating emerging experimental results with these criteria, this review establishes a framework for designing encapsulation strategies that reconcile mechanical and barrier demands.

Stretchable and flexible optoelectronic devices are increasingly integrated into daily life, serving as light-emitting diodes (LEDs) displays in mobile electronics and home appliances, as well as energy harvesting modules such as solar cells and indoor photovoltaics (PVs)[1–8]. As application domains expand, the mechanical requirements have evolved beyond simple bending and folding to more complex deformation modes, including uniaxial/biaxial stretching, twisting, and conformal wrapping over curved surfaces[9–12]. In general, mechanical flexibility denotes the ability of a device or material to undergo reversible shape deformation under externally applied forces, representing the opposite of rigidity. In the context of flexible electronics, flexibility is typically associated with bending and folding deformation, where curvature accommodates the deformation and tensile strain on the most brittle layer can be minimized through neutral-plane engineering. Devices that deform predominantly through bending-dominated modes, with only small tensile strain at the outer surface on the order of 1%, are therefore classified as mechanically flexible. By contrast, stretchability requires all constituent layers in the device to deform cooperatively under an iso-strain condition. Stretchable systems can sustain large tensile deformation (>5–50%) under uniaxial or biaxial loading and support more complex shape reconfigurations such as conformal wrapping. Achieving stretchability consequently demands intrinsic material strategies and extrinsic structural designs that suppress crack initiation and delamination under significant tensile strain, fundamentally distinguishing it from bending-dominated flexibility[9]. Figure 1 shows representative applications of interactive optoelectronic devices: wearable solar cell, electronic skin (e-skin), head-up display (HUD), stretchable displays, and rollable space solar cell. Wearable devices with self-energy harvesting systems like wearable organic solar cells (OSCs) can sustain continuous operation of the device (Fig. 1a)[13], and e-skin platforms are capable of sensing healthcare information and presenting the data via integrated display (Fig. 1b)[14]. HUDs, integrated into curved windshields of automobiles or aircraft, enable augmented reality (AR) navigation and speed readouts without obstructing the

---

[1]Department of Materials Science and Engineering, UNIST (Ulsan National Institute of Science and Technology), Ulsan, Republic of Korea. [2]UNIST InnoCORE AI-Space Solar Initiative, UNIST (Ulsan National Institute of Science and Technology), Ulsan, Republic of Korea. [3]Graduate School of Semiconductor Materials and Devices Engineering, UNIST (Ulsan National Institute of Science and Technology), Ulsan, Republic of Korea. [4]John A. Paulson School of Engineering and Applied Sciences, Harvard University, Cambridge, MA, USA. [5]Department of Materials Science and Engineering, Seoul National University, Seoul, Republic of Korea. [6]These authors contributed equally: Hyeonji Yoo, So-Hyeon Lee. ✉e-mail: juyoung@unist.ac.kr

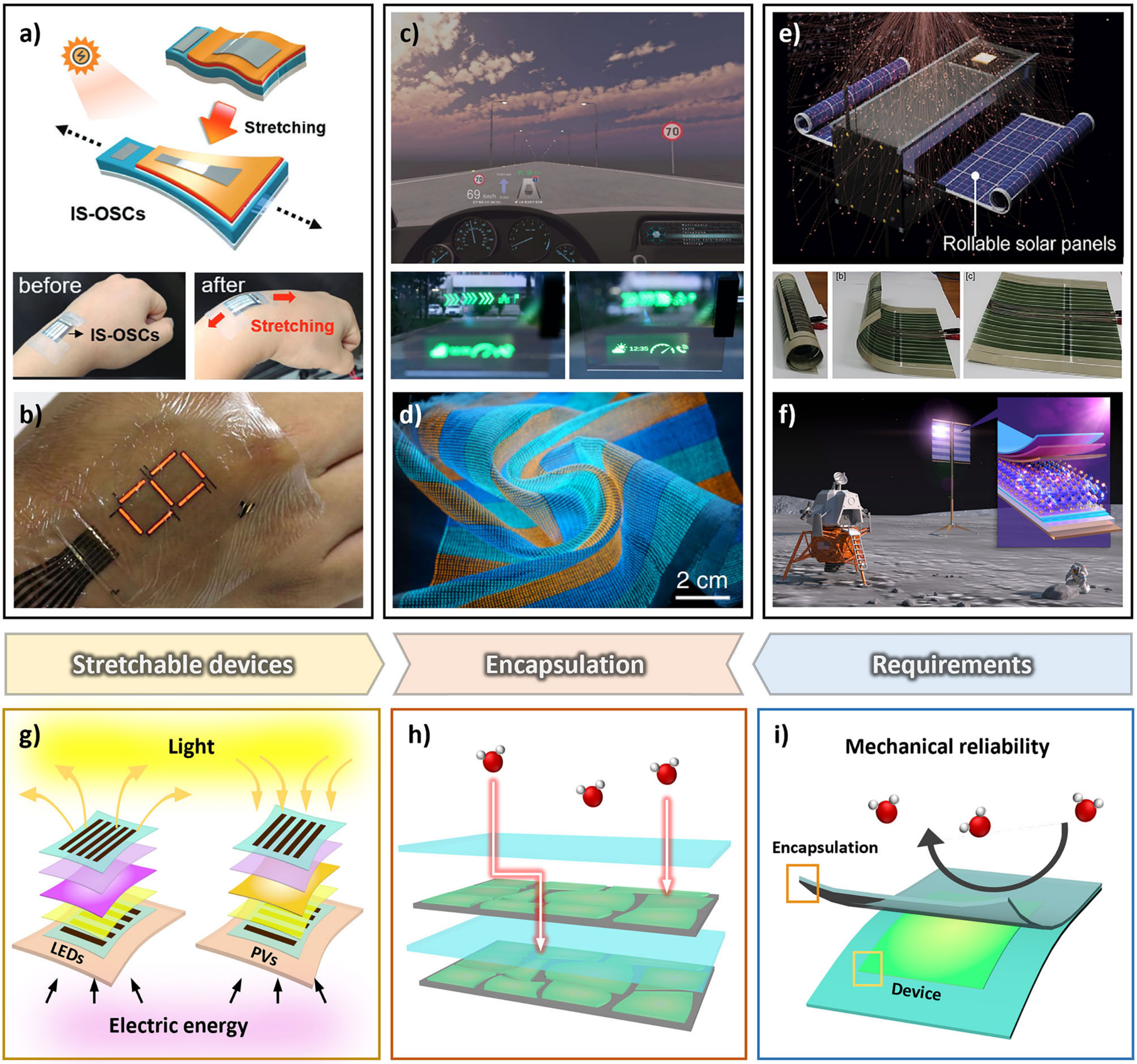

Fig. 1 | Representative present and future stretchable and flexible optoelectronics. a Schematic and images of wearable OSC during stretching mode. Adapted with permission from ref. 13. Copyright 2022, Wiley-VCH GmbH. **b** Operation image of wearable e-skin on hand. Reproduced with permission from ref. 14. Copyright 2016, The Authors. **c** Schematic and images of AR HUD for automobiles. Reproduced with permission from refs. 15,16. Copyright 2023, Human Factors and Ergonomics Society. Copyright 2022, Optica Publishing Group. **d** Crumpled stretchable display based on textile substrate. Reproduced with permission from ref. 17. Copyright 2021, The Authors. **e** Schematic and images of rollable solar panels for space electronics. Reproduced with permission from ref. 18. Copyright 2024, American Chemical Society. **f** Schematic of solar panel operation on the Moon. Reproduced with permission from ref. 19. Copyright 2023, American Chemical Society. **g** Schematic of the structure of stretchable optoelectronic devices: LEDs and PVs. **h** Water vapor penetration path in a hybrid encapsulation material. **i** Requirements for stretchable encapsulation.

driver's field of view (Fig. 1c)[15,16]. Stretchable free-form displays, envisioned for televisions and smartphones, combine enhanced portability with seamless integration into diverse surfaces (Fig. 1d)[17]. For space-deployable PVs, rollable panel formats facilitate compact packaging for launch and efficient deployment for solar harvesting in orbit (Fig. 1e, f)[18,19]. Collectively, these applications highlight the growing demand for optoelectronic devices with highly stretchable, unconstrained form factors. To meet these requirements, both (i) intrinsic strategies, which rely on the inherent deformability of functional materials, and (ii) extrinsic strategies, which employ engineered structures such as buckles (e.g., wavy or wrinkled geometries), meta-structures, and island–bridge layouts to accommodate strain through structural design, have been explored[20–25]. These advances have enabled stretchable LED and PV systems with high optical and electrical performance, as illustrated in Fig. 1g.

Soft organic materials play a pivotal role in enabling advanced form factors and driving commercialization of stretchable and flexible optoelectronics. While conventional metallic electrode materials are too rigid for stretchable platforms, they have been replaced by conductive polymers (e.g., poly(3,4-ethylenedioxythiophene):poly(styrene sulfonate) (PEDOT:PSS)) or conductive nanomaterial-polymer composites (e.g., silver nanowires (Ag NWs), graphene-embedded polymers)[26,27]. Their intrinsic compliance further supports the development of stretchable substrates, dielectric layers, and active photosensitive layers capable of withstanding repeated mechanical deformation. Nevertheless, these advantages come with intrinsic trade-offs. Organic materials generally exhibit low glass-transition temperatures and high chemical reactivity toward moisture and oxygen, even under ambient conditions. Such instabilities result in accelerated environmental degradation, thereby imposing strict limitations on the thermal budget and atmospheric controls required during fabrication. Moreover, they restrict the range of operational environments where devices can perform reliably.

To ensure long-term stability under practical operating conditions, encapsulation is indispensable. As the outermost protective layer, it shields active components from moisture, oxygen, and other environmental stressors while preserving the mechanical compliance required for stretchable and flexible devices[28–30]. As shown in Fig. 1h, an effective encapsulation layer increases the diffusion pathway for penetrating water molecules, thereby slowing their transport toward moisture-sensitive layers. Conventional encapsulation approaches in optoelectronic devices have relied heavily on dense, rigid materials such as ultrathin glass (UTG) sheets or metal lids to prevent water vapor and oxygen penetration into the photoactive components. While these configurations provide robust environmental protection in rigid or curved systems, their intrinsic brittleness and inability to accommodate large deformations make them fundamentally incompatible with stretchable devices. For reliable operation in stretchable and flexible optoelectronics, encapsulation must function as a stand-alone, mechanically adaptive barrier capable of deforming in concert with the device while preserving high optical transmittance[31,32]. Achieving this combination of properties is challenging, owing not only to the intrinsic trade-off relation between stretchability and barrier performance, where increased elongation generally degrades barrier performance, but also to the need for low-temperature processing compatible with heat-sensitive components. Moreover, encapsulation requirements vary across applications. PV devices require high optical transmittance to maximize light absorption, and LEDs must also maintain high transmittance for efficient light out-coupling. Space-deployable solar cells operate in moisture-free environments but are subjected to intense ultraviolet (UV) radiation and extreme thermal cycling, necessitating encapsulation materials with exceptional radiation resistance and thermal stability[33,34]. Reliable encapsulation strategies that satisfy device-specific requirements, environmental conditions, and target lifetimes are therefore critical for achieving systems that maintain both mechanical reliability and robust barrier performance, as depicted in Fig. 1i.

We provide a comprehensive overview of recent progress in encapsulation technologies engineered for stretchable and flexible optoelectronics, categorized by material—organic, inorganic, and hybrid materials—as well as their associated fabrication methodologies. Organic barriers generally exhibit superior mechanical deformability, allowing them to accommodate large strains, but their limited gas barrier capability due to low density constrains long-term device stability. In contrast, inorganic barriers possess intrinsically low gas permeability and great chemical resistance, yet their brittleness and poor strain tolerance often lead to fracture or delamination under deformation. Hybrid encapsulation systems, integrating organic and inorganic materials, have been developed to balance these opposing characteristics, offering both mechanical adaptability and enhanced environmental protection. This review highlights the importance of strategically integrating material selection, encapsulation methods, and application requirements to address the intrinsic trade-off between barrier performance and mechanical stretchability. Recent advances are analyzed to define the key performance parameters required for reliable operation and to propose design strategies that support the development of next-generation encapsulation systems. These strategies are expected to accelerate the advancement of stretchable optoelectronic devices from laboratory prototypes to mechanically robust and environmentally stable devices suitable for commercial applications.

Barrier performance and stretchability of encapsulation materials

To apply encapsulation to stretchable and flexible electronic devices, encapsulation materials should simultaneously provide high barrier performance and high deformability. Since the required barrier and mechanical performance levels vary depending on the device type, it is essential to identify these requirements for the intended application[28,29,35,36]. As the barrier and mechanical properties are intrinsic to the encapsulation material, understanding the fundamental characteristics of candidate materials is a prerequisite for rational selection. As illustrated in Fig. 2a, the permeation of water vapor and oxygen is strongly governed by the microstructure and density of free volume within the material. Polymer-based materials have abundant free volume and large macro-defects, allowing comparatively fast penetration of a significant amount of moisture within a given time frame. Polycrystalline inorganic materials possess ordered lattices, but grain boundaries and nanoscale defects act as rapid diffusion pathways for moisture. In contrast, amorphous metals and oxides lack grain boundaries and exhibit disordered atomic arrangements, then defects do not form continuous pathways but instead create tortuous diffusion paths. Accordingly, the selection of encapsulation materials requires careful consideration of their barrier properties in relation to their structural characteristics.

Barrier performance is generally evaluated by the water vapor transmission rate (WVTR) and oxygen transmission rate (OTR). Although OTR quantifies oxygen permeability, WVTR is more widely adopted because water molecules diffuse more rapidly than oxygen due to smaller molecule size and higher reactivity and induce more severe degradation of device performance. Therefore, WVTR has become the primary benchmark for encapsulation performance under environmental stress. In addition to barrier performance, stretchability represents another essential requirement for encapsulation materials in stretchable devices. Mechanical performance is generally evaluated through bending, twisting, folding, and stretching tests; among these, stretchability is regarded as the most representative measurement for highly deformable devices, while bending is often used for weakly deformable devices. Figure 2b compares the WVTR and stretchability ranges across organic, inorganic, and hybrid encapsulation materials, and Table 1 summarizes representative properties reported in recent literature[21,22,28,29,31,37–50]. In Fig. 2b, organic, inorganic, and hybrid materials occupy the yellow, blue, and green regions, respectively, while blue stars denote structure-assisted inorganic films (e.g., wrinkled and wavy SiO_2) whose enhanced stretchability arises from geometry-enabled strain accommodation rather than intrinsic material deformability. Hybrid materials, which combine the barrier integrity of inorganic layers with the mechanical compliance of organic components, represent a key strategy for achieving encapsulation systems that balance low WVTR with moderate stretchability. In parallel, structure-assisted designs offer a complementary pathway by enabling geometry-driven deformability without compromising barrier performance. These material- and structure-centered approaches outline promising routes toward next-generation stretchable encapsulation technologies.

To evaluate the practical relevance of encapsulation strategies, it is essential to consider not only the numerical WVTR values but also how they translate to real operating conditions. While WVTR serves as the primary descriptor of barrier performance, its implications must be contextualized in terms of device lifetime and environmental exposure. For most optoelectronic devices operated under ambient conditions, WVTR values in the range of 10^{-4}–10^{-6} g/m²·day are generally accepted as the minimum threshold for long-term stability[36,51,52]. These values become more intuitive when expressed in terms of macroscopic leakage. If a film the size of a soccer field was used as encapsulation and exposed to water for one month, the amount of water penetrating with no barrier would be equivalent to a large tanker truck. A WVTR of 10^{-1} g/m²·day—typical of food-packaging-grade polymer films—would reduce this to roughly a bottle of water. A WVTR of 10^{-4} g/m²·day, suitable for OPVs, corresponds to only a spoonful of water, while the OLED benchmark of 10^{-6} g/m²·day represents the leakage of just a single droplet. These requirements vary widely depending on device architecture, expected service lifetime, and operating environment. In high-humidity regions such as tropical rainforests, enhanced barrier performance is necessary due to increased moisture concentration and elevated water

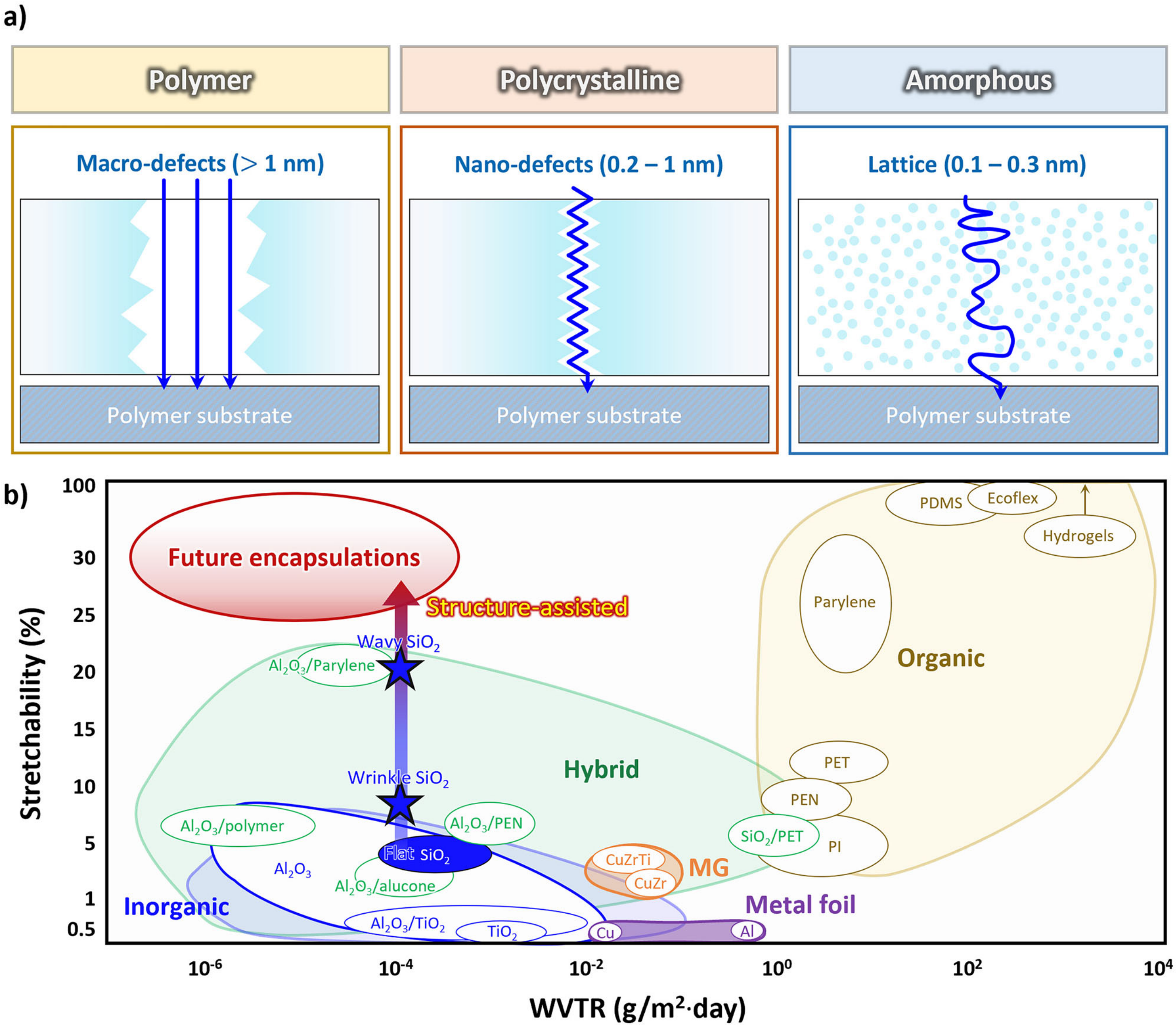

Fig. 2 | Water vapor transmission pathways and performance of encapsulation materials. **a** Schematic illustration of water vapor transmission pathways through microstructures in encapsulation materials on a polymer substrate. The encapsulation materials have macro-defects (left), nano-defects (center), and atomic lattice spacing (right). **b** Overview of WVTR–Stretchability performance for common encapsulation materials[21,22,28,29,31,37–50,55,77,103,135,136]. The design space for organic (yellow), inorganic (blue), and hybrid (green) encapsulation materials is shown. The blue star denotes SiO$_2$, an inorganic material whose stretchability is improved through a structure-assisted design. Structural assistance enables low permeability encapsulation materials to maintain low WVTR while achieving enhanced deformability, highlighting a potential pathway for next-generation stretchable and flexible encapsulation strategies.

diffusivity in the ambient atmosphere. Lifetime requirements for such environments are commonly assessed using accelerated environmental tests (e.g., 85 °C/85% relative humidity (RH)), combined with Arrhenius extrapolation of lag time and WVTR values measured at multiple temperatures to estimate diffusion activation energy and permeance[22,47]. This allows prediction of barrier performance under target field conditions. Accordingly, encapsulation thickness and material selection must be tailored for the intended environment, and reliability verified under accelerated conditions. While WVTR provides a universal metric for air-exposed optoelectronic devices, it does not directly translate to encapsulation requirements for implantable or underwater systems, where degradation is dominated by liquid-phase water ingress and surface chemical reactions rather than water vapor diffusion. For such cases, alternative metrics—such as water transmission rate (WTR) or operational lifetime in liquid environments—and dedicated testing methods are required[53,54]. Therefore, selecting appropriate measurement methodologies that reflect the dominant moisture-penetration mechanisms for each application is critical, and reliability should be evaluated through accelerated tests that can be extrapolated to practical use conditions. Detailed methodologies and measurement strategies are discussed in the following section.

Representative organic materials include polyethylene naphthalate (PEN), polyimide (PI), polydimethylsiloxane (PDMS), parylene and hydrogels[4,28,37,41,42,55–68]. These materials generally show WVTR values on the order of 10^{-1}–10^{2} g/m^2·day, indicating poor barrier performance, insufficient for stand-alone encapsulation, but providing superior stretchability and low elastic modulus. As shown in Fig. 2b, such polymers are advantageous for highly stretchable devices because their mechanical compliance minimizes strain mismatch with active layers. They also offer advantages in processability, as they can be fabricated through spin-coating, solution-based methods, chemical vapor deposition (CVD), and so on. For these reasons, organic materials are primarily applied in devices requiring high stretchability rather than extreme environmental resistance. Design strategies often involve encapsulating devices between polymer encapsulation layers or controlling layer thickness to align the active region with the mechanical neutral plane, thereby reducing strain-induced damage and enhancing durability.

Table 1 | Summary of encapsulation materials including organic, inorganic, and hybrid materials in stretchable and flexible optoelectronic devices

Type	Materials	Fabrication method	Structure	Stretchability	Thickness [µm]	WVTR (condition) [g/m²·day]	Elastic modulus [GPa]	Application	Ref.
Organic	PET	Spin-coating	Single	12%	>1.4	7.9 (75 µm) (38 °C/90%RH)	2.3	OLED	28,29
	PDMS	Spin-coating	Single	93%	>4	65–70 (38 °C/90%RH)	(0.4–5) × 10^{-3}	Skin electronics	28,29,37
		Emulsification + curing	Microsphere	N/D	2 (diameter)	- (7 days)	N/D	PQD, PNC	38
	PI	Spin-coating	Single	3% (w/ device)	>0.5	2.2	2.5	PLED	28,29,39
		Spin-coating	Serpentine (w/ etching)	30% by serpentine (w/ device)	3.5 (w/ device)	N/D	N/D	Body temperature sensor	40
	Parylene	CVD	Single	R_b: 0.25–13 mm	1	Operation in water droplet	N/D	PeLEDs	41,42
		CVD	Wrinkle	60% by wrinkle (w/ device)	2–10	29.8 (2 µm) (36 °C/ 75%RH)	0.23–0.36 (w/ device)	Strain sensor	43
	PEN	Spin-coating	Single	7%	>1.2	7.3 (100 µm)	3.3	Transparent electronics	28,29
	SBS	Spinning	Single (Nanofiber)	N/D	<26	800	0.1 × 10^{-3}	Skin electronics	134
	SEBS	Solvent casting	Single	N/D	250	5 (1 mm) (38 °C/90% RH)	3.2 × 10^{-3}	Strain sensor	56
	Ecoflex	Spin-coating	Single	~90%	400	132.2 (400 µm) (36 °C/80% RH)	68.9 kPa	Strain sensor	43
	SIBS	Solvent casting	Single	800%	1000	0.24 (1 mm) (38 °C/ 90% RH)	10^{-3}	Skin-like electronics	114
	SVS	Solvent casting	Single	800%	1000	0.095 (1 mm) (38 °C/ 90% RH)	1.1 × 10^{-3}	Skin-like electronics	114
	Hydrogel	3D printing	Single	150% (w/ device)	200 (w/ device)	N/D	$10^{-0.5}$	N/D	44
Inorganic	Al_2O_3	PEALD	Single	3.09%	50 × 10^{-3}	3.21 × 10^{-4} (60 °C/ 85%RH)	179.6	OSC, OLED	45
	Al_2O_3 /TiO_2	ALD	Nanolaminate	0.53%	90–110 × 10^{-3}	9.48 × 10^{-5}	55.6–61.7	OLED	46
	SiO_2	Thermal growth	Wavy	20.1% by wavy	2 × 10^{-1}	2.25 × 10^{-4} (55 °C/ 85%RH)	69.01	OLED, OPV	22
		Thermal growth	Wrinkle	5 ~ 9% by wrinkle (biaxial)	2 × 10^{-1}	2.9 × 10^{-4} (60 °C/ 85%RH)	73.8	OLED, OPV	21
		Sol–gel	Single	3.3%	2 × 10^{-1}	2.9 × 10^{-4} (60 °C/ 85%RH)	61	OSC	47
Hybrid	Al_2O_3/PDMS	ALI/spin-coating	Nanolaminate	50 cycles at R_b: 5 mm	35 × 10^{-3}/22	9.24 × 10^{-5} (3 dyads) (25 °C/50%RH)	200/2.28 × 10^{-3}	OLED	48
	pV3D3/Al_2O_3	iCVD/ALD	Nanolaminate	40% (w/ device)	0.16/60 × 10^{-3}	N/D	N/D	OLED	49
	Montromorillonite/NOA	Self-assembly processing	Nanolaminate	1000 cycles at R_b: 2 mm	NOA: 10	6.66 × 10^{-3} (2 dyads) (25 °C/40%RH)	0.628	PLED, PSC	31
	PCL/SiO_2 flakes	Solvent casting	Flakes in polymer	>150%	100	35 (100 µm) (25 °C/50%RH)	>0.5	LED	50

Inorganic materials such as Al_2O_3, SiO_2, TiO_2, and ZrO_2 generally achieve WVTR values in the range of 10^{-3}–10^{-6} g/m²·day, reflecting excellent barrier performance[21,22,39,45,47,52,69]. However, despite these advantages in barrier properties, inorganic materials have inherent mechanical limitations[70]. They exhibit limited strain tolerance caused by high elastic modulus, and low fracture strain, restricting their application in stretchable systems. Defects such as pinholes readily propagate within these films, and even small applied strains can induce brittle fracture, causing a rapid deterioration of barrier performance. Film thickness can be another critical design parameter. Increasing thickness can reduce permeation by extending the diffusion path, but at the expense of flexibility and with a higher risk of crack formation under bending or stretching[71]. Therefore, inorganic materials could be optimized to remain in the ultrathin regime, often only a few tens of nanometers, to balance barrier performance with mechanical compliance. Another important factor is the elimination of atomic-scale defects and the fabrication of dense microstructures to ensure barrier integrity, which can act as crack-propagation origins and high-diffusion pathways. Conventional physical vapor deposition (PVD) and CVD have been widely employed to fabricate inorganic films.

In contrast, atomic layer deposition (ALD) and atomic layer infiltration (ALI) have been widely employed to produce uniform and defect-rare inorganic layers[72–74]. Although these processes can yield dense, low-defect inorganic films with excellent barrier integrity, their inherently slow growth rates limit large-area scalability and require additional process innovations for commercial implementation. One practical pathway adopted in industry involves forming a polymer or CVD-derived base layer first, followed by deposition of an ultrathin ALD or ALI coating, which preserves film compactness while reducing overall process time. Continued optimization of such hybrid deposition schemes is therefore essential to achieving both manufacturing efficiency and structural integrity. Within the broader ALD/ALI framework, plasma-enhanced ALD (PEALD) offers higher deposition rates at lower temperatures, which is advantageous for thermally fragile polymer substrates[75,76]. In addition, ALI enables direct infiltration of inorganic precursors into polymer substrates, creating interpenetrated hybrid interfaces that enhance both barrier performance and strain tolerance. These substrate-assisted approaches remain within the domain of inorganic encapsulation but also represent transitional pathways toward hybrid encapsulation strategies, as they utilize polymer compliance to mitigate defect formation and fracture. Consequently, while inorganic materials remain indispensable for applications requiring extremely high barrier performance under harsh environments, their practical use in highly stretchable electronics is limited unless combined with hybrid or structural strain-accommodation approaches.

As discussed above, organic materials are vulnerable to moisture and oxygen penetration, whereas inorganic materials exhibit limited strain tolerance. To overcome these intrinsic limitations, hybrid encapsulation systems integrating both materials have been investigated[31,32,46,48–50,77–86]. Most hybrid encapsulation materials typically adopt multilayer configurations, in which inorganic layers provide high barrier performance, while organic layers suppress crack propagation and accommodate mechanical strain. This configuration effectively generates a tortuous diffusion pathway for moisture and oxygen, enabling WVTR values in the intermediate range of 10^{-1}–10^{-5} g/m²·day, superior to pure polymers yet more mechanically compliant than dense inorganic films[46,87]. The performance advantage arises from the complementary roles of each constituent. Inorganic layers act as the primary gas barriers, whereas organic layers serve as stress-relief and defect-sealing components, preventing catastrophic crack growth during deformation. Representative structural designs include alternating dyads such as Al_2O_3/polymer and SiO_2/polymer laminates[31,48–50], which maintain low WVTR while accommodating moderate strain, making them suitable for stretchable optoelectronic applications. In hybrid materials, beyond classical nanolaminate stacks, composite-type hybrid systems have been developed in which high-aspect-ratio inorganic fillers (e.g., graphene oxide, Al_2O_3 nanosheets) are dispersed within a polymer matrix. These fillers substantially increase the tortuosity of diffusion paths, thereby reducing permeability, while preserving bulk stretchability because the fillers are embedded in the compliant matrix rather than forming continuous brittle films.

However, for fabrication of hybrid materials, the implementation of hybrid materials requires careful thermal and chemical compatibility control. Organic materials typically possess low glass transition temperatures (T_g) and are prone to thermal degradation, limiting the feasibility of high-temperature inorganic deposition[87,88]. Therefore, low-temperature techniques such as PEALD and ALI have been employed. In particular, ALI enables precursor infiltration into the subsurface of the polymer, filling free volume and increasing density without compromising the bulk compliance[48]. This approach reduces permeation pathways, strengthens interfacial adhesion, and improves both barrier performance and long-term reliability. Overall, hybrid encapsulation offers a balanced compromise between impermeability and mechanical compliance. By combining multilayer nanolaminate structures, polymer–inorganic composite designs, and low-temperature deposition processes, hybrid strategies represent a leading pathway toward achieving low WVTR and high stretchability for next-generation deformable optoelectronics[31,50,80].

In parallel, structural engineering approaches, including serpentine, island–bridge, wrinkled, and metamaterial geometries, have been employed to further enhance the stretchability of encapsulation–device systems[20–22,81,89]. Pre-straining or depositing inorganic layers on patterned substrates can induce wrinkle or wavy morphologies that improve strain accommodation in brittle oxides such as SiO_2[21,22]. As shown in Fig. 2b, wavy or wrinkled SiO_2 layers exhibit significantly greater stretchability than flat films while retaining low WVTR. These results highlight that coupling low-permeability inorganic or hybrid barriers with structural modifications is a promising route for realizing stretchable encapsulation layers. Detailed research progress on each class of encapsulation material will be discussed in the following sections.

Evaluation of barrier performance in stretchable and flexible optoelectronic devices

The impermeability of encapsulation materials is commonly assessed using three representative techniques: the coulometric sensor-based method, the electrical calcium (Ca) test, and the optical Ca test. Among these, the coulometric sensor-based method quantifies the WVTR by electrochemically detecting the moisture that permeates through the encapsulation layer[90,91]. As illustrated in Fig. 3a, the specimen is positioned between wet and dry chambers, thereby establishing a concentration gradient that drives water vapor transport. The transmitted vapor is absorbed by an electrochemical sensor and subsequently decomposed, generating a current proportional to the amount of permeated moisture. This technique, widely adopted in commercial systems such as the MOCON instrument (ASTM F1249), provides high reproducibility with a detection resolution down to 5×10^{-3} g/m²·day. However, its sensitivity remains insufficient for probing the ultra-low WVTR levels on the order of 10^{-5}–10^{-6} g/m²·day, which are critical for ensuring long-term reliability in high-performance stretchable and flexible optoelectronic devices.

The electrical Ca test determines WVTR by exploiting the high reactivity of Ca toward oxidation by water vapor[31]. As illustrated in Fig. 3b, a thin Ca sensing layer is deposited beneath the encapsulation layer and exposed to a controlled humid environment. Water vapor permeating through the barrier oxidizes Ca, decreasing its thickness and increasing its electrical resistance. By continuously monitoring the resistance change, the rate of Ca consumption can be quantified, and be used to calculate the WVTR[48]. The mass transport rate of water vapor, R_w, and the mass consumption rate of Ca by water vapor, R_{Ca}, are expressed as:

$$R_w = WVTR \cdot A_B, \tag{1}$$

$$R_{Ca} = R_w \left(\frac{M_{Ca}}{M_w}\right) \frac{1}{n}, \tag{2}$$

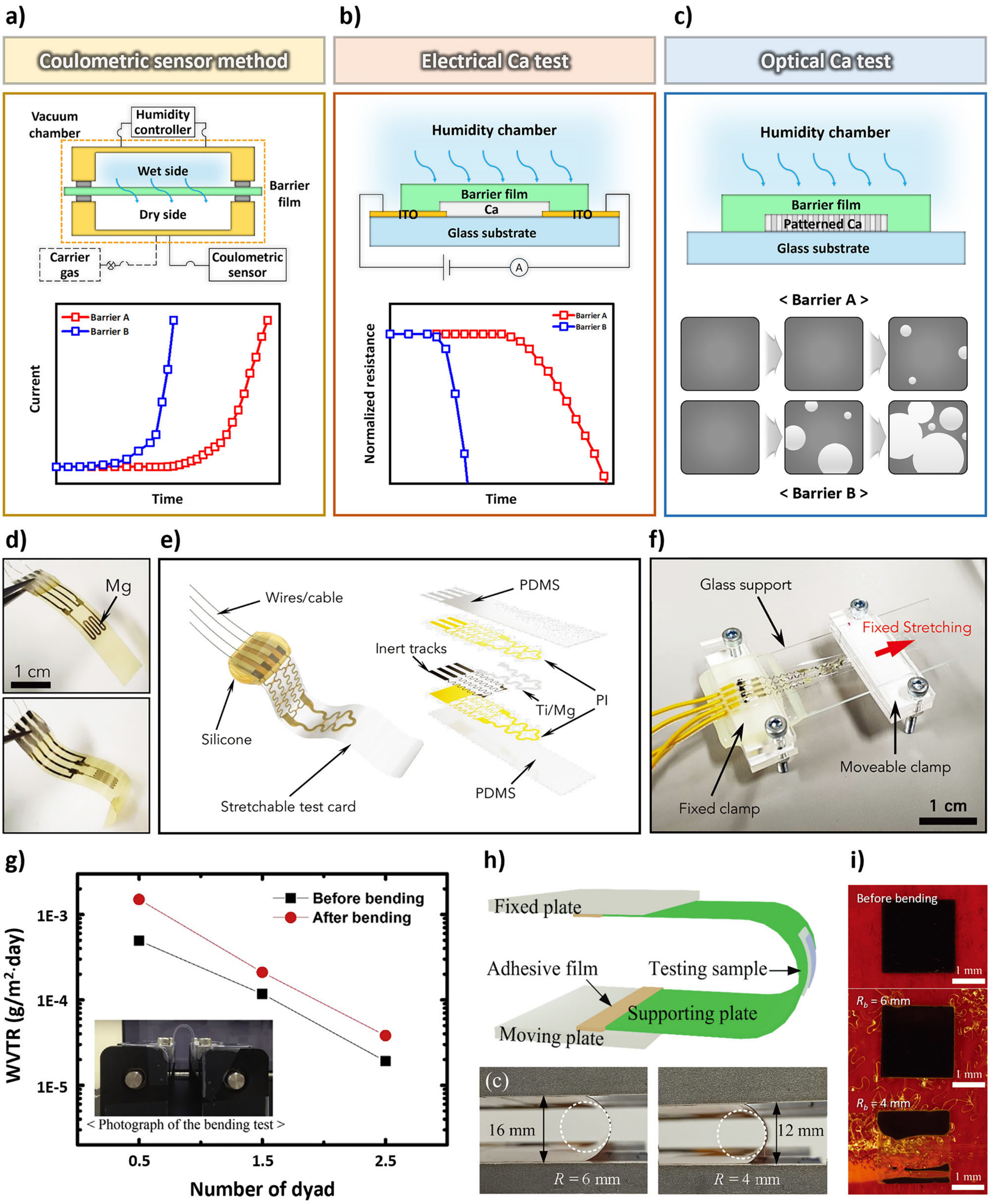

Fig. 3 | Measurement methodologies of barrier performance in encapsulation materials. Schematic of the method and corresponding results for **a** a coulometric sensor-based method, **b** electrical Ca test, and **c** optical Ca test. Images of **d** flexible and **e** stretchable electrical Mg test cards. **f** Stretching test setup for in-situ WVTR measurement with fixed strain. Reproduced with permission from ref. 95. Copyright 2024, The Authors. **g** Results of ex-situ WVTR measurement before and after bending test of hybrid encapsulation. Adapted with permission from ref. 96. Copyright 2016, Elsevier B.V. **h** Schematic and photographs of the cyclic bending test. **i** Results of optical Ca test at 60 °C/85% RH condition. Adapted with permission from ref. 47. Copyright 2022, Tsinghua University Press.

where A_B is the barrier film area, M_{Ca} and M_w are the molar masses of Ca and water, respectively, and n is the number of water molecules reacting per Ca atom. In the reaction, $Ca + 2H_2O \rightarrow Ca(OH)_2 + H_2$, two water molecules react with one Ca atom, giving $n = 2$. For a thin Ca film, R_{Ca} can be expressed as:

$$R_{Ca} = A_{Ca}\delta\left(\frac{dh}{dt}\right), \tag{3}$$

where A_{Ca} is the Ca sensor area, δ is the density of Ca, h is the Ca film thickness, and t is time. Substituting Eqs. (1)–(3), WVTR is obtained as:

$$WVTR = n\delta\left(\frac{A_{Ca}}{A_B}\right)\frac{M_w}{M_{Ca}}\frac{dh}{dt}. \tag{4}$$

The resistance of Ca senor, R is calculated by:

$$R = \frac{\rho_{Ca} l_{eff}}{wh}, \tag{5}$$

where ρ_{Ca} is the resistivity of Ca, l_{eff} is the effective length of the Ca sensor, and w is the sensor width. Since h is proportional to $\frac{1}{R}$, $\frac{dh}{dt}$ can be written as:

$$\frac{dh}{dt} = -\frac{\rho_{Ca} l_{eff}}{w} \cdot \frac{d\left(\frac{1}{R}\right)}{dt}. \tag{6}$$

Then, WVTR can be determined as follows:

$$WVTR = n\delta\rho_{Ca}\left(\frac{l_{eff}}{w}\right)\left(\frac{A_{Ca}}{A_B}\right)\frac{M_w}{M_{Ca}}\frac{d\left(\frac{1}{R}\right)}{dt}. \tag{7}$$

Since Ca exhibits high sensitivity to water vapor, it enables WVTR measurements with a resolution as low as 1×10^{-6} g/m^2·day. In some cases, magnesium (Mg) is employed as an alternative reactive sensing layer due to its relatively easy handling and compatibility for fabricating stretchable test cards, while maintaining comparable moisture reactivity.

While the electrical Ca test enables quantitative determination of the WVTR, the optical Ca test provides a qualitative evaluation of barrier performance, particularly useful for detecting and tracking the evolution of pinhole-type defects. These defects serve as high-diffusion pathways for water vapor, leading to accelerated degradation of barrier functionality. In this method, a Ca layer or pattern is deposited beneath the encapsulation; when water vapor penetrates through pinholes, the underlying Ca undergoes oxidation, causing a distinct change in optical properties from opaque to transparent. This transformation increases the optical transmittance of the film, thereby allowing direct visualization and mapping of defect initiation and propagation over time. As illustrated in Fig. 3c, the optical Ca test effectively reveals localized oxidation patterns, especially under bending strain that promotes pinhole formation[45]. Although inherently qualitative, this technique offers valuable insights into the spatial distribution and mechanical origins of barrier failure, complementing the quantitative data obtained from the electrical Ca test.

Conventional WVTR measurement techniques are typically conducted using rigid test fixtures. However, stretchable and flexible optoelectronic devices are inherently exposed to repetitive or static mechanical deformation during operation, which can critically influence encapsulation barrier reliability. Accordingly, measuring WVTR under relevant deformation modes is essential to more accurately represent practical device conditions. The deformation setup and testing parameters are generally tailored to the encapsulation material system—whether organic, inorganic, or hybrid—as well as to the environmental and mechanical demands of the targeted application. Stretchability and flexibility are commonly characterized in terms of applied strain, bending radius, and the number of stretching or bending cycles. WVTR measurements under mechanical deformation can be performed using either in-situ or ex-situ approaches. In-situ protocols enable real-time monitoring of WVTR during the application of mechanical strain, thereby capturing the strain-dependent onset of impermeability degradation. Despite this advantage, their applicability is constrained by complex experimental setups and limited test conditions. As a result, ex-situ methods are more widely employed, wherein WVTR is measured before and after mechanical deformations. This decoupling of encapsulation barrier evaluation from mechanical deformations greatly simplifies the experimental process, but it cannot track the progressive nature of degradation in encapsulation barrier during deformation. In ex-situ protocols, cyclic bending or stretching is applied to simulate long-term operational stresses, after which the specimen is returned to standard measurement conditions. The comparison of WVTR values obtained before and after deformations provides quantitative insight into the durability limits and mechanical tolerance of encapsulation systems.

In cyclic stretching tests, the applied strain is typically calculated from the longitudinal extension of the specimen. However, because most materials exhibit a positive Poisson's ratio, stretching is accompanied by transverse shrinkage. This effect becomes particularly critical in organic materials with high Poisson's ratios and in optoelectronic devices where the active area directly governs performance[92–94]. In addition, during stretching or bending tests, improper gripping can induce tearing or localized damage, often arising from unsuitable sample geometries or excessive clamping forces. To mitigate these issues, strategies such as optimizing sample mounting geometries and employing compliant or rigid supporting plates have been introduced to reduce grip-induced artifacts[47]. Careful control of such experimental variables is essential not only for accurately assessing mechanical durability but also for enabling reliable cross-comparisons of barrier performance across different material systems.

Recent studies have investigated organic, inorganic, and hybrid encapsulation materials to elucidate how their distinct mechanical and barrier properties evolve under practical operating conditions. Organic encapsulation layers, in particular, offer high mechanical compliance and stretchability, rendering them attractive for highly deformable optoelectronic devices. Their durability is often assessed under demanding strain conditions. For example, stretchable electrical Mg test cards have been developed for in-situ WVTR monitoring under controlled temperature and humidity (Fig. 3d–f), enabling real-time observation of degradation in encapsulation barrier during stretching or bending[95]. Nevertheless, most studies continue to rely on ex-situ approaches in which WVTR is measured using rigid test fixtures before and after mechanical loading. As illustrated in Fig. 3g, cyclic bending tests with a 30 mm radius over 1000 cycles followed by WVTR measurements at 30 °C/90% RH provide a direct comparison of barrier integrity before and after deformation[96]. These complementary approaches collectively highlight the trade-off between experimental simplicity and the ability to capture the dynamic progression of degradation in encapsulation barrier. Inorganic encapsulation materials inherently provide low WVTR and chemical inertness, making them highly effective diffusion barriers. However, their intrinsic brittleness often leads to cracking or delamination under mechanical deformation, thereby restricting their applicability in stretchable optoelectronic devices. To overcome these limitations, sol–gel processes have been explored to fabricate flexible SiO_2 films, aiming to combine the excellent barrier performance of inorganics with enhanced mechanical compliance[47]. Cyclic bending tests were carried out using a setup in which the bending radius was controlled by adjusting the distance between two plates (Fig. 3h). The barrier performance was then evaluated using both electrical and optical Ca tests under 60 °C/85% RH conditions before and after 50,000 bending cycles (Fig. 3i), demonstrating the feasibility of tailoring inorganic coatings for mechanically durable encapsulation.

Hybrid encapsulation strategies combine an organic matrix with inorganic fillers or laminated organic/inorganic films to simultaneously achieve high stretchability and low WVTR. For instance, Al_2O_3-infiltrated PDMS films have been examined under 1% strain for 1000 cyclic stretching tests, with WVTR evaluated before and after deformation at 25 °C/85% RH using the electrical Ca test. To overcome the limitations of ex-situ measurements—which cannot capture the real-time progression of barrier degradation—WVTR was further monitored after 0, 10, 100, and 1000 stretching cycles[89]. These studies reveal that small bending radii or prolonged static strain can induce localized cracking within the inorganic sublayers, leading to modest increases in WVTR. Nevertheless, the surrounding polymer matrix effectively suppresses catastrophic barrier failure. Taken together, hybrid encapsulation approaches offer a practical compromise, delivering both mechanical robustness and effective moisture protection for stretchable optoelectronic devices.

Stretchable organic encapsulation materials

Organic encapsulation materials constitute the most widely adopted approach for achieving intrinsic stretchability because they inherently possess low elastic modulus, high elongation, and the ability to accommodate large deformations without structural failure. These mechanical advantages enable organic encapsulation layers to withstand diverse deformation modes, including stretching-dominant modes, while maintaining device integrity, making them highly suitable for stretchable optoelectronic devices. During tensile loading, all constituent layers of a device typically experience an iso-strain condition; thus, minimizing mechanical mismatch between layers is critical for preserving mechanical reliability. In contrast, when rigid materials are used as constituent materials, disparities in mechanical properties such as elastic modulus and Poisson's ratio give rise to interfacial stress concentrations. Under cyclic deformation, these localized stresses can initiate delamination and accelerate crack propagation, ultimately compromising device stability and operational lifetime. Mechanically compliant organic encapsulation layers mitigate these issues by dissipating applied strain more uniformly, thereby reducing interfacial stress and suppressing crack propagation. Structural stability can be further enhanced by positioning brittle functional layers close to the neutral mechanical plane, which minimizes strain during bending and stretching[55,57]. To this end, device designs often balance the thicknesses of the substrate and encapsulation to form symmetric architectures that protect the active layers and extend operational lifetimes.

Representative organic encapsulation materials include PDMS, Ecoflex, and parylene, which are selected according to device-specific requirements such as neutral plane engineering, optical transmittance, and barrier performance[41,58–60]. As shown in Fig. 4a, a skin-attachable, high-efficiency pure-red perovskite LED (PeLED) was encapsulated with a 1.4 μm parylene overlayer and integrated on a parylene/epoxy substrate (1 μm/600 nm)[42]. The device maintained stable operation even in the presence of surface water. By positioning the brittle indium tin oxide (ITO) electrode at the neutral plane through optimized control of substrate and encapsulation thicknesses, strain concentration was effectively mitigated. This design enabled stable optical and electrical performance under humid conditions and during bending with radii ranging from 0.25 mm to 13 mm. Collectively, these results highlight that parylene encapsulation, combined with neutral plane engineering, not only ensures reliable operation under bending deformation but also enables conformal integration with curved surfaces such as human skin.

Polyurethane acrylate (PUA), exhibiting a WVTR of 28.9 g/m²·day and an elastic modulus of 3.2 GPa, has been utilized as both the substrate and the encapsulation layer, thereby enabling neutral-plane design while providing mechanical robustness[62]. This PUA sandwich architecture effectively minimized interfacial stress mismatches and protected active layers from excessive strain. As a result, intrinsically stretchable quantum dot LEDs (QLEDs) maintained stable luminance without notable degradation under tensile strains up to 50%. Furthermore, a 5 × 5 passive-matrix QLED array demonstrated consistent operation when deformed from a flat configuration to a convex geometry (Fig. 4b)[4]. Under 30% strain, the device exhibited its characteristic strain-dependent luminance response arising from strain-induced thickness reduction, and this intrinsic behavior was preserved without distortion or suppression. The PUA encapsulation maintained the electroluminescent characteristics of the device during mechanical deformation, underscoring its effectiveness in sustaining optoelectronic performance during stretching (Fig. 4c).

Achieving high luminance from inherently elastic LEDs remains a significant challenge. To address this, an all-polymer LED (APLED) was developed by introducing a nano-constrained light-emitting polymer structure, formed through spontaneous phase separation of an elastomer within the emissive layer, thereby creating distinct elastic and emissive domains that preserved optical performance while imparting stretchability (Fig. 4d)[63]. The device employed a drop-cast poly(styrene-ethylene/butylene-styrene) (SEBS) substrate laminated between poly(styrene-isobutylene-styrene) (SIBS) encapsulation layers, which provided low oxygen and moisture permeability[56]. With a low elastic modulus of 1 MPa, this configuration enabled bright and uniform emission under bending and stretching, supporting real-time skin-mounted display operation. In another approach, PDMS, with a WVTR of 65 g/m²·day and an elastic modulus of 0.9 MPa, was utilized as both the substrate and encapsulation layer, offering high compliance and allowing the mechanically fragile layer to be positioned near the neutral plane[28,64]. This configuration reduced crack initiation under high strain and preserved both structural integrity and barrier performance. When combined with hybrid electrodes composed of Ag NWs embedded in a PEDOT:PSS matrix and sandwiched between bilayer graphene films, this encapsulation strategy enabled the fabrication of a large-area stretchable alternating-current electroluminescent (ACEL) device. As shown in Fig. 4e, the encapsulated ACEL device maintained excellent electroluminescent performance under various mechanical deformations—including bending, twisting, and stretching—and retained stable operation at uniaxial strains up to 80% (Fig. 4f)[37]. These results underscore that careful selection and design of organic encapsulation layers, in combination with hybrid electrode architectures, can provide reliable and bright performance in highly deformable LEDs.

In both LED and PV devices, operational stability is inseparable from encapsulation performance. In PV devices, penetration of moisture and oxygen directly reduces the power conversion efficiency (PCE) and fill factor (FF), making effective barrier design indispensable. Fiber-compatible solar cells, which provide continuous power for wearable systems, require robust encapsulation to prevent degradation from environmental exposure. As illustrated in Fig. 4g, an ultra-flexible organic PV (OPV) device with a total thickness of 3 μm was fabricated on a parylene/epoxy (1 μm/500 nm) substrate. An additional 1 μm parylene overlayer was deposited as encapsulation, and the device was laminated on both sides with pre-stretched acrylic elastomer (3 M VHB, 500 μm) to enhance elasticity and water resistance. This approach addressed the relatively high elastic modulus (4 GPa) and poor WVTR (90 g/m²·day) of parylene[65]. Positioning the active layer at the neutral plane further minimized mechanical strain during deformation. As shown in Fig. 4h, the double-sided elastomer-coated OPV exhibited negligible changes in FF even under 52% compressive strain. Moreover, after 20 compressive cycles at 52% strain, the device retained 83% of its initial PCE, demonstrating high mechanical durability and reliable performance under cyclic deformation.

As shown in Fig. 4i, an ultra-thin flexible perovskite solar cell was developed with improved stability under ambient conditions and encapsulated with a 1 μm polyurethane (PU) layer deposited by spray coating for mechanical protection[66]. The freestanding perovskite array, with a total thickness of 3 μm, delivered a unit-weight power output of 23 W/g with encapsulation and 26 W/g without encapsulation, demonstrating outstanding power-to-weight efficiency. Stretchability was achieved by transferring the device onto a pre-stretched acrylic elastomer (3 M VHB), enabling subsequent compression and re-extension. The pre-strain of the elastomer, together with the bending stiffness of the solar cell, induced sinusoidal wrinkles and high-aspect-ratio bridge structures, allowing stable operation under 50% uniaxial compression corresponding to 100% tensile strain (Fig. 4j). When laminated onto a radially pre-stretched elastomer, the device formed a random two-dimensional wrinkle network with complex topography, maintaining structural stability and preserving photovoltaic performance under 44% area reduction.

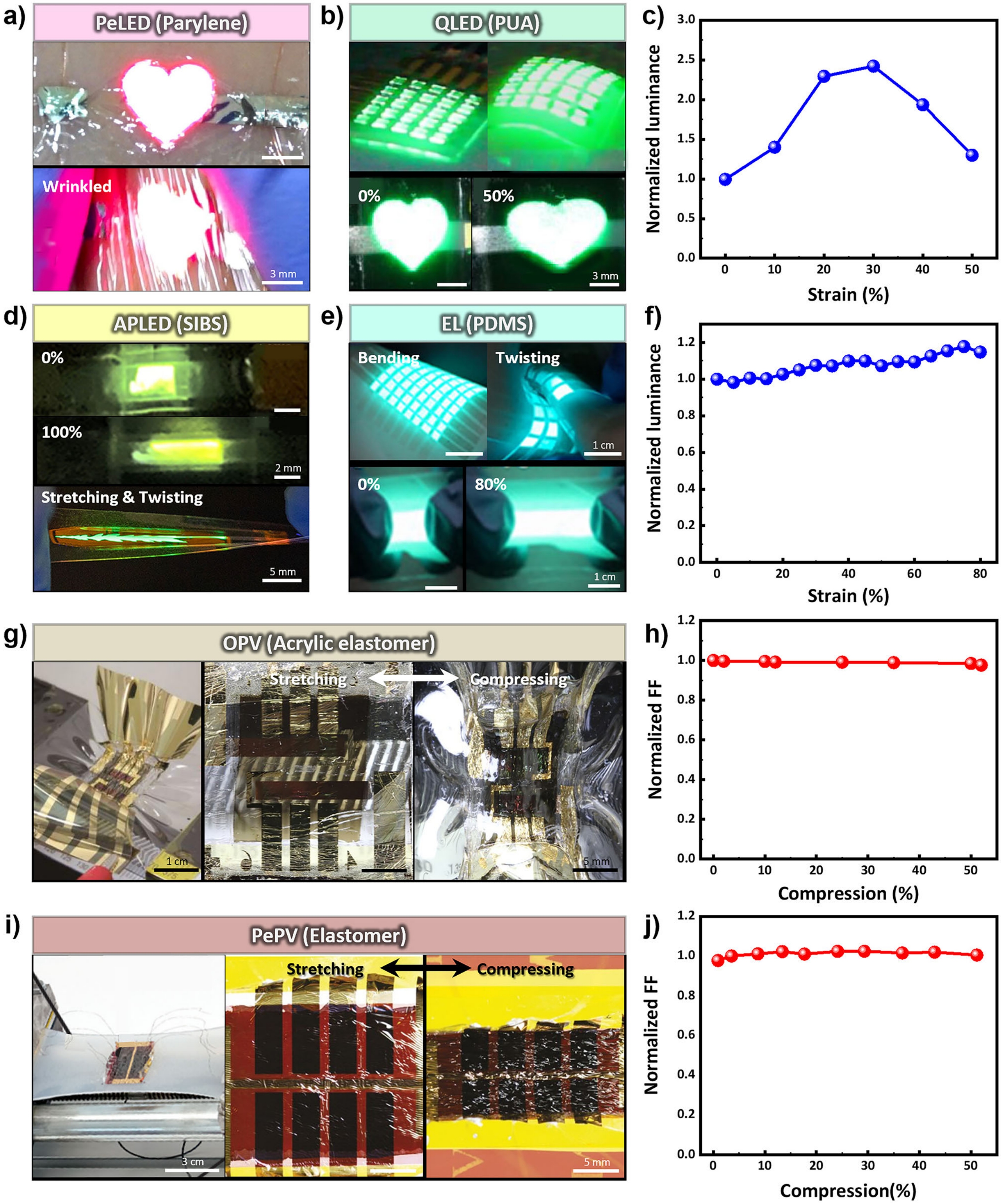

Fig. 4 | Stretchable optoelectronic devices using organic encapsulation materials. **a** Ultrathin, skin-attachable PLEDs encapsulated with parylene in a flat state (top) and in a wrinkled state (bottom). Adapted with permission from ref. 42. Copyright 2024, Elsevier Ltd. **b** Intrinsically stretchable QLEDs array encapsulated with PUA in a flat and convex mode (top) and stretched up to 50% strain (bottom). **c** Normalized luminance of QLED as a function of applied strain. Adapted with permission from ref. 4. Copyright 2024, The Authors. **d** Stretchable APLEDs encapsulated with SIBS stretched up to 100% (right) and a patterned, stretchable light-emitting polymer film under simultaneous stretching and twisting (bottom). Adapted with permission from ref. 63. Copyright 2022, The Authors. **e** Stretchable EL array encapsulated with PDMS under bending and twisting (top) and an EL pixel unit stretched up to 80% strain (bottom). **f** Normalized luminance of stretchable EL devices as a function of applied strain. Adapted with permission from ref. 37. Copyright 2019, American Chemical Society. **g** Uniaxial compression of stretchable and waterproof OPVs up to 49% by release of elastomers. **h** Normalized FF of OPVs as a function of applied compression. Adapted with permission from ref. 65. Copyright 2017, The Authors. **i** Uniaxial compression of lightweight, high–power–density PSCs with release of elastomers up to 50%. **j** Normalized FF of PSC as a function of applied compression. Adapted with permission from ref. 66. Copyright 2015, Springer Nature.

Organic material–based substrates and encapsulation layers offer distinctive advantages in elasticity, conformability, and lightweight integration. However, their relatively high WVTR values (10^{-1}–10^{2} g/m²·day), arising from low density and macro-scale defects, remain a critical limitation for long-term device stability[67,97]. Their barrier performance can further change under mechanical deformation through several mechanisms. Bending or stretching increases the free volume within the polymer network, which facilitates molecular diffusion and elevates the WVTR. Polymers with a Poisson's ratio near 0.5 undergo significant thickness reduction under large tensile strain, shortening the effective diffusion path and accelerating moisture penetration into active layers. In semi-crystalline polymers, mechanical strain can also induce chain and lamellar alignment along the stretching direction, altering the tortuosity of diffusion pathways and leading to direction-dependent moisture transport[98]. These deformation-induced structural changes modify the intrinsic barrier performance of organic encapsulation layers, underscoring the importance of evaluating their barrier properties under relevant mechanical deformation conditions when assessing suitability for stretchable devices. Increasing the encapsulation thickness can improve barrier properties almost linearly, but the associated stiffness increases cubically with thickness, resulting in a pronounced loss of flexibility and stretchability[68,99]. This fundamental trade-off has motivated recent research into inorganic encapsulation strategies that can combine superior barrier performance with mechanical resilience.

Flexible inorganic encapsulation materials

Inorganic encapsulation materials have been primarily developed for bending-dominant flexible devices rather than for highly stretchable platforms, owing to their high elastic modulus and intrinsically brittle nature. Inorganic thin films are prone to crack initiation and propagation under tensile strain, fundamentally limiting their applicability under stretching-dominant deformation. Nevertheless, their key advantage lies in achieving ultralow permeability under small-strain conditions. Because barrier performance critically depends on suppressing direct permeation pathways and promoting tortuous diffusion routes, both strongly influenced by intrinsic defects and free volume, inorganic encapsulation strategies have focused on amorphous oxides, which achieve ultralow WVTR by eliminating continuous diffusion channels[46,100]. For optoelectronic applications, optical transparency is additionally required, with representative amorphous oxides including SiO_x, AlO_x, SiN_x, TiO_x, and ZnO. Dense and highly transparent amorphous thin films have been fabricated using deposition techniques such as ALD, and sol–gel processing, while more recent approaches employ ALI to construct multilayer architectures. Through these methods, both single-layer and multilayer oxide thin films have achieved WVTR values in the range of 10^{-3}–10^{-6} g/m²·day under ambient conditions, demonstrating their effectiveness in ensuring the long-term reliability of organic optoelectronic devices. Beyond these representative systems, ongoing research has expanded to diverse inorganic materials that offer complementary strategies to mitigate defect-driven permeation while simultaneously enhancing durability under mechanical strain and harsh environmental conditions. Such developments underscore the potential of inorganic encapsulation approaches to provide robust barrier performance without compromising optical or mechanical functionality.

Amorphous oxides are representative inorganic encapsulation materials, offering ultralow WVTR due to their strong atomic bonding, low reactivity with water molecules, and the absence of grain boundaries that act as high-diffusion pathways in polycrystalline films. As shown in Fig. 5a, high-density SiO_x layers prepared by sol–gel processing clearly demonstrate these advantages[47]. In this process, metal alkoxide precursors form a colloidal sol that is subsequently dried and thermally treated to create a three-dimensional oxide network. A final high-temperature annealing step at 1000 °C eliminates residual porosity, yielding films with density and moisture permeation activation energies comparable to fused silica. Under cyclic bending tests of up to 50,000 cycles at 85 °C/85% RH with an applied strain of 3.3%, the WVTR of the annealed SiO_x layers remained unchanged. This exceptional stability indicates that densification suppresses the formation of defect nucleation sites such as pinholes, resulting in defect-scarce thin films that retain barrier integrity even under prolonged cyclic deformation.

While high-temperature annealing is commonly employed in sol–gel processes, encapsulation films for stretchable and flexible devices are generally deposited directly onto plastic or elastomer substrates, which strictly limits the allowable processing temperature. To address this challenge, amorphous AlO_x encapsulation films have been successfully fabricated by PEALD at process temperatures between 50 °C and 80 °C[45]. Optical calcium testing confirmed that low-temperature-deposited amorphous Al_2O_3 layers maintained stable WVTR values after 100,000 bending cycles at $R_b = 25$ mm (0.25% strain) under 85 °C/85% RH. However, strain-dependent degradation was evident under more severe bending conditions. At $R_b = 10$ mm (0.6% strain), significant pinhole formation was observed after only 1000 cycles, while at $R_b = 20$ mm (0.3% strain), fine pinholes appeared after 100,000 cycles, leading to a sharp increase in WVTR (Fig. 5b). This degradation is attributed to atomic bond rearrangements in the amorphous network, where dangling Al–O bonds and residual hydroxyl groups reorganize under mechanical stress to generate pinhole defects that act as rapid permeation pathways.

To mitigate pinhole-induced diffusion, multilayer architectures have been widely adopted. By sealing or decoupling localized defects, multilayer barriers compel water molecules to follow longer, more tortuous diffusion paths, thereby enhancing overall barrier performance. A representative example is the composite structure combining ALD Al_2O_3 with graphene[69]. In this approach, graphene was synthesized by CVD on Cu foil, transferred onto PEN substrates after Cu removal, and subsequently functionalized with NO_2 groups to facilitate conformal oxide deposition. Al_2O_3 layers with thicknesses of 25 and 50 nm were then deposited on the NO_2-functionalized graphene using ALD. Graphene functionalization resulted in denser oxide films and a significant reduction in surface roughness—from 4.432 to 0.539 nm—compared with Al_2O_3 layers deposited without functionalization. The encapsulation performance of the composite was evaluated by electrical calcium testing under 85 °C/85% RH. Compared with individual Al_2O_3 and graphene layers, as well as single Al_2O_3 films of varying thickness, the Al_2O_3/graphene composite exhibited markedly superior barrier properties, achieving a WVTR of 2.62×10^{-4} g/m²·day and showing signs of degradation only after 53 h. As shown in the inset of Fig. 5c, organic LEDs (OLEDs) encapsulated with the Al_2O_3/graphene composite remained operational after 24 h of continuous operation. Furthermore, after cyclic bending tests, the composite barrier demonstrated higher mechanical durability and flexibility compared with single Al_2O_3 layers. The improved encapsulation is attributed to the impermeable aromatic ring structure of graphene, which effectively suppresses water permeation at the Al_2O_3 interface. Although graphene may contain local defects, its conjugated carbon network remains intrinsically impermeable to water molecules, thereby complementing and reinforcing the barrier effect of the oxide layer.

Nanolaminate thin films provide an additional strategy to improve barrier durability under combined thermal and humidity stress[96,101,102]. Al_2O_3/MgO (AM) nanolaminate thin films fabricated by ALD, together with silica nanoparticle–embedded sol–gel organic–inorganic nanocomposites, were assembled into a 2.5-dyad multi-barrier architecture. Flexible OLEDs (FOLEDs) encapsulated with AM nanolaminate barriers exhibited stable operation under 0.63% strain for 1000 cycles and maintained luminance for over 50 days at 60 °C/90% RH (Fig. 5d). Under these harsh conditions, the WVTR increased only slightly—from 1.7×10^{-5} to 6.9×10^{-5} g/m²·day (Fig. 5e)[103]. The enhanced durability is attributed to the hygroscopic nature of MgO, which mitigates hydrolysis of Al_2O_3, and to the formation of interfacial aluminate phases that suppress water and oxygen diffusion along grain boundaries. These synergistic effects highlight the potential of nanolaminate designs to achieve reliable barrier performance in flexible optoelectronic devices.

In addition to nanolaminate thin films, doped oxide multilayers have been developed to provide multifunctional encapsulation. A ZnO-based

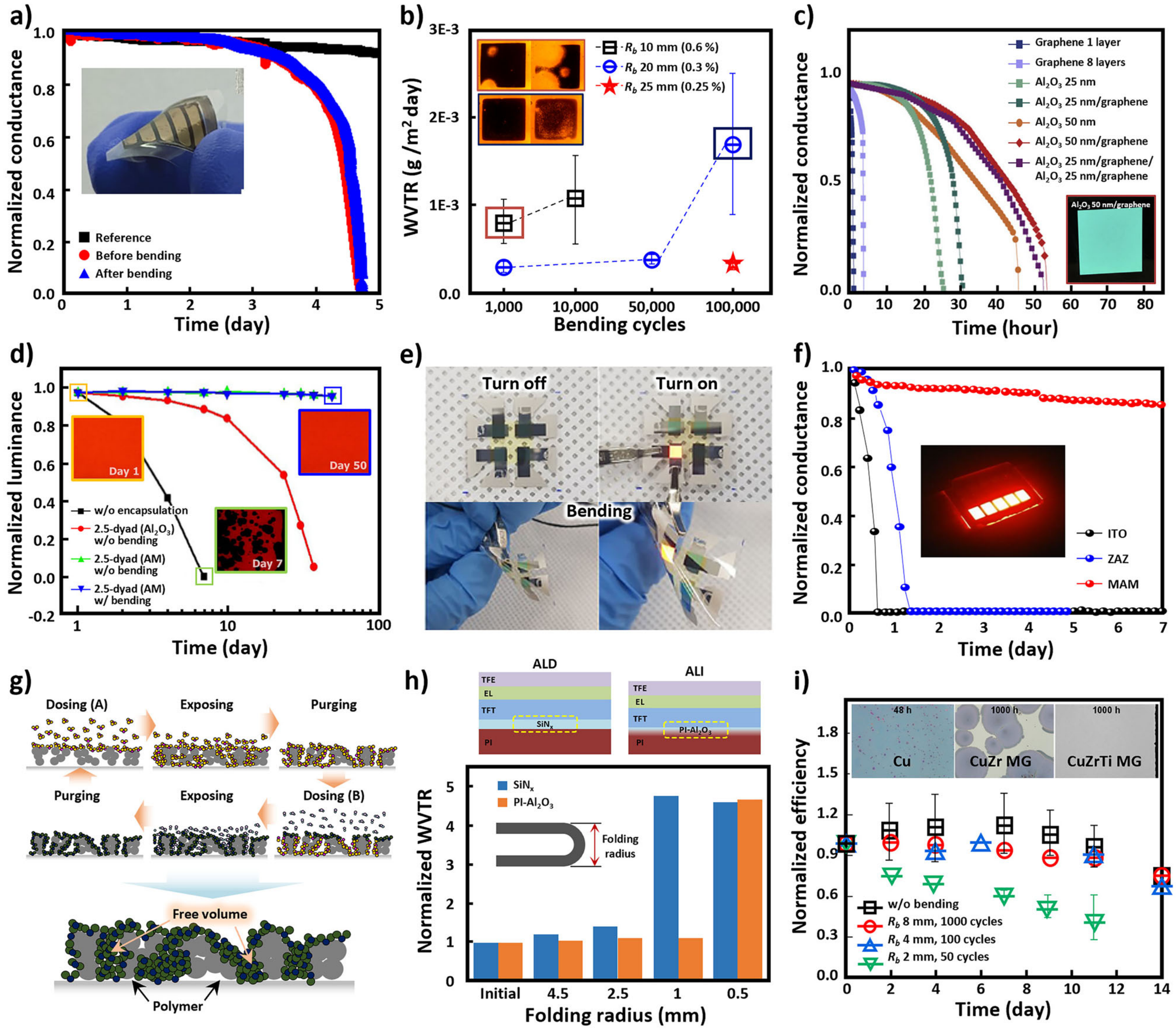

Fig. 5 | Flexible optoelectronic devices using inorganic encapsulation materials. **a** Normalized conductance for WVTR measurement of sol–gel silica films before and after 50,000 bending cycles at 6 mm radius under 60 °C/85% RH, with encapsulated OSC inset. Adapted with permission from ref. 47. Copyright 2022, Tsinghua University Press. **b** WVTR results and stereoscopic microscopy images after optical Ca tests following cyclic bending tests. Adapted with permission from ref. 45. Copyright 2021, American Chemical Society. **c** Normalized conductance from electrical Ca test of graphene, Al_2O_3 and Al_2O_3/graphene encapsulation, with OLED demonstration inset. Adapted with permission from ref. 69. Copyright 2017, Elsevier Ltd. **d** Normalized luminance of FOLEDs without encapsulation, with a 2.5-dyad Al_2O_3 multi-barrier, and with a 2.5-dyad AM multi-barrier under shelf-lifetime bending testing under 60 °C, 90% RH, and **e** corresponding device images. Adapted with permission from ref. 103. Copyright 2020, Tsinghua University Press and Springer-Verlag GmbH Germany, part of Springer Nature. **f** Normalized conductance for WVTR measurement of ITO, ZAZ and MAM structures under 30 °C/90% RH, with red-emitting MAM-based OLED inset. Adapted with permission from ref. 104. Copyright 2018, American Chemical Society. **g** Schematic of ALI process. **h** Normalized WVTR as a function of folding radius for ALD-inorganic layer and PI-Al_2O_3 hybrid layers through ALI. Adapted from ref. 39. Available under a CC-BY 4.0 license. Copyright 2022, The Authors. **i** Normalized efficiency of flexible OSCs with CuZrTi MG encapsulation under various bending radius and cycles, and optical microscope (OM) images after environmental test under 85°C/85% RH. Adapted with permission from ref. 107. Copyright 2022, American Chemical Society.

multilayer structure doped with Al and Mg (MgO/Al_2O_3/ZnO, MAZO) was fabricated by ALD, in which ZnO layers were periodically intercalated with MgO and Al_2O_3 doping layers[104]. The incorporation of dopants suppressed ZnO crystallization, reduced grain boundary density, and increased the packing density of the amorphous matrix, thereby forming a gas-diffusion multibarrier that effectively blocked the permeation of moisture and oxygen. Under accelerated testing at 30 °C/90% RH, electrical calcium measurements revealed WVTR values of 2.41×10^{-1} g/m^2·day for conventional indium tin oxide (ITO) electrodes and 8.31×10^{-2} g/m^2·day for ZnO/Ag/ZnO (ZAZ) multilayers. By contrast, the MAZO/Ag/MAZO (MAM) structure exhibited a markedly reduced WVTR of 9.2×10^{-5} g/m^2·day (Fig. 5f). This outstanding barrier performance is attributed to both the suppression of ZnO crystal growth and the creation of multiple interfacial layers that hinder diffusion pathways. As a result, MAM multilayers demonstrated excellent resistance to device degradation and ensured long-term operational stability. These multifunctional films underscore an integrated encapsulation strategy that simultaneously serves as a transparent electrode and a protective passivation layer, thereby expanding the design space for high-performance OLEDs.

Beyond multilayer inorganic approaches, further improvements have been realized by enhancing the interaction between inorganic films and polymer substrates. ALI has emerged as a promising strategy to form inorganic layers within polymer substrates with improved defect tolerance and flexibility. The ALI process is derived from conventional ALD but incorporates an additional exposure step between dosing and purging[72]. During this step, precursor and reactant molecules are allowed sufficient time to diffuse into and penetrate the free volume of the polymer substrate. Through this infiltration, voids that could otherwise act as permeation pathways for moisture and oxygen are effectively filled with Al_2O_3 (Fig. 5g). ALI-grown Al_2O_3 films on PI substrates exhibited significantly enhanced barrier performance[39]. WVTR measurements using the tritium method showed that bare PI substrates had values of 2.2 g/m²·day, whereas PI–Al_2O_3 films achieved 1.4×10^{-5} g/m²·day. This dramatic reduction indicates that infiltrated Al_2O_3 effectively blocks permeation pathways and markedly strengthens the moisture barrier function. Mechanical durability was further assessed via folding tests (Fig. 5h). Conventional SiN_x films fabricated by ALD showed a sharp increase in WVTR at a folding radius of 1 mm, attributed to crack formation in the brittle oxide layer that facilitated water penetration. In contrast, PI–Al_2O_3 films maintained stable WVTR down to a folding radius of 1 mm, with increases observed only at 0.5 mm. These findings highlight the superior flexibility and defect tolerance enabled by interfacial interactions between inorganic films and polymer substrates. While such substrate-assisted strategies remain within the domain of inorganic encapsulation, they also represent a transitional approach bridging toward hybrid encapsulation architectures, where inorganic films directly infiltrate or integrate with polymer matrices.

While oxide thin films are widely employed for flexible encapsulation owing to their high barrier performance and tunable multilayer architectures, metal foils have also been utilized on the non-transparent side of flexible devices. Aluminum, copper, and stainless-steel foils exhibit moderately low WVTR values on the order of 10^0–10^{-2} g/m²·day, thereby extending device lifetime[105–107]. When applied to non-illuminated regions, metal foils not only simplify device architectures but also block unwanted light leakage[105]. However, their limited flexibility necessitates laminated or hybrid configurations with polymer substrates for practical use in deformable systems. Despite these constraints, metal-foil encapsulation remains a viable strategy for applications requiring hermetic sealing and structural stability under specific design conditions. Metallic glasses (MGs) provide an alternative approach to metal-foil encapsulation. Unlike polycrystalline metal foils, which contain grain boundaries that act as high-diffusion pathways, MGs are amorphous and exhibit high corrosion resistance under ambient conditions. CuZrTi MG thin films, in particular, demonstrate superior moisture resistance under high-temperature and high-humidity environments, attributed to their disordered atomic configuration that suppresses continuous permeation channels[107]. Uniform and dense CuZrTi films can be deposited by magnetron sputtering at low processing temperatures. Under accelerated testing at 85 °C/85% RH for 1000 h, nanocrystalline Cu and binary CuZr films underwent rapid surface oxidation, whereas CuZrTi films retained their amorphous structure with negligible corrosion (Fig. 5i). When integrated as encapsulation layers in organic solar cells, CuZrTi MG films preserved more than 90% of the initial device efficiency after 11 days of cyclic bending at a radius of 4 mm, underscoring their combined advantages of high barrier performance and mechanical robustness.

Organic/inorganic hybrid encapsulation materials toward stretchable encapsulation

Hybrid encapsulation materials, which integrate organic and inorganic layers into multilayer or composite architectures, have emerged as an effective strategy for achieving highly impermeable yet stretchable encapsulation. By combining the complementary properties of each constituent, these systems maintain reliable barrier performance while sustaining mechanical deformability required for stretchable devices. In these multilayer configurations, dense inorganic layers serve as the primary barrier against moisture ingress, whereas the intervening organic layers enhance mechanical compliance by accommodating and dissipating applied strain while simultaneously sealing defects in the inorganic layers[46,48,78,79,83,108]. This synergistic interaction increases overall tortuosity, thereby improving barrier performance while retaining mechanical flexibility. In addition to the physical stacking arrangement, the long-term reliability of hybrid encapsulation is strongly influenced by the chemical and mechanical compatibility at the organic-inorganic interfaces. Accordingly, effective interface engineering is required to maximize the synergistic effects of these architectures and support the stable operation of stretchable devices.

Representative structure and process are shown in Fig. 6a, where alumina (A, 60 nm) was deposited by ALD and silamer (S, 550 nm), a silane-based polymer, was spin-coated as the organic layer[78]. Repeating this deposition-coating sequence formed uniform Al-Si-O interfacial bonds, improving both barrier performance and tensile properties in the free-standing state. The optimized 2.5-dyad SASAS structure achieved a maximum elongation of 2.8% with high ductility through structural engineering and robust interface (Fig. 6b). The silamer layer effectively dissipates strains and stabilizes crack propagation in the alumina layers, as further verified by WVTR measurements under bending. Under 1% bending strain, SASAS structure maintained a WVTR on the order of 10^{-3} g/m²·day, whereas ASASA exceeded 10^{-1} g/m²·day (Fig. 6c). In fiber-based wearable OLEDs with SASAS encapsulation preserved 99% of initial luminance after 250 hours of operation and 88% after water immersion for 24 h and applying 1% of bending strain. These results imply the excellent moisture resistance and mechanical robustness of the SASAS multilayer, highlighting its potential for next-generation stretchable optoelectronic applications.

Barrier performance can be further enhanced by increasing the number of interfaces and incorporating more than binary hybrids by suppressing defect connectivity. Nanolaminate structures, created by alternately depositing inorganic sublayers, suppress the growth of pinhole-like defects and decouple defects. In ALD-deposited Al_2O_3/ZrO_2 (2.6 nm/3.6 nm) nanolaminates, amorphous Al_2O_3 terminates ZrO_2 crystallite growth, while ZrO_2 prevents the accumulation of unreacted Al-OH species, limiting the extension of voids in the Al_2O_3 layer[102]. Furthermore, the dense $ZrAl_xO_y$-aluminate mixed phase formed at sublayer interfaces effectively blocks gas diffusion, enabling a 130 nm nanolaminate to achieve a predicted WVTR of 5×10^{-7} g/m²·day under ambient condition.

Although higher ALD process temperatures can improve film quality, direct encapsulation of organic devices requires processing below 70 °C due to their low glass transition temperature[109]. Therefore, low-temperature ALD is particularly suitable for these thermally fragile systems. Extending this consideration to practical implementation, Al_2O_3/TiO_2 nanolaminates were deposited at 40 °C for direct encapsulation of OLEDs[85]. This inorganic layer, composed of 3 nm sublayers (ATN3, N, 30 nm), exhibited a WVTR of 9×10^{-4} g/m²·day under 30 °C/90% RH condition, outperforming single-layer Al_2O_3 and TiO_2 as shown in Fig. 6d. To induce hybrid effects, a silamer layer (S, 1 μm) was spin-coated, serving as both a planarization layer and a mechanical buffer layer, while a parylene C overlayer (P, 3 μm) was applied as the hydrophobic outermost barrier to enhance environmental stability. The resulting NSNSP hybrid encapsulation achieved an ultralow WVTR of 9×10^{-6} g/m²·day, reflecting the combined effects of nanolaminate engineering, organic buffering, and hydrophobic surface modification. In these hybrid multilayer systems, positioning organic layers at the top and bottom places brittle inorganic layers closer to the neutral plane, thereby enhancing mechanical stability and promoting uniform strain energy dissipation. Under this configuration, the 2.5-dyad of SNSNS structure achieved a maximum elongation of 2.74% as shown in Fig. 6e. Furthermore, an OLED device encapsulated bilaterally at the top and bottom exhibited an elongation of 2.03% and maintained its initial luminance for approximately 32 days, whereas a device without top encapsulation showed continuous luminance degradation under ambient conditions.

The performance of hybrid multilayers is also strongly governed by the organic-inorganic interfacial properties. To reinforce interfacial binding, a strategy has been developed in which the inorganic layer is partially infiltrated into the organic matrix via the ALI process. This resulted graded infiltration zone of mixed composition rather than a sharp interface is a

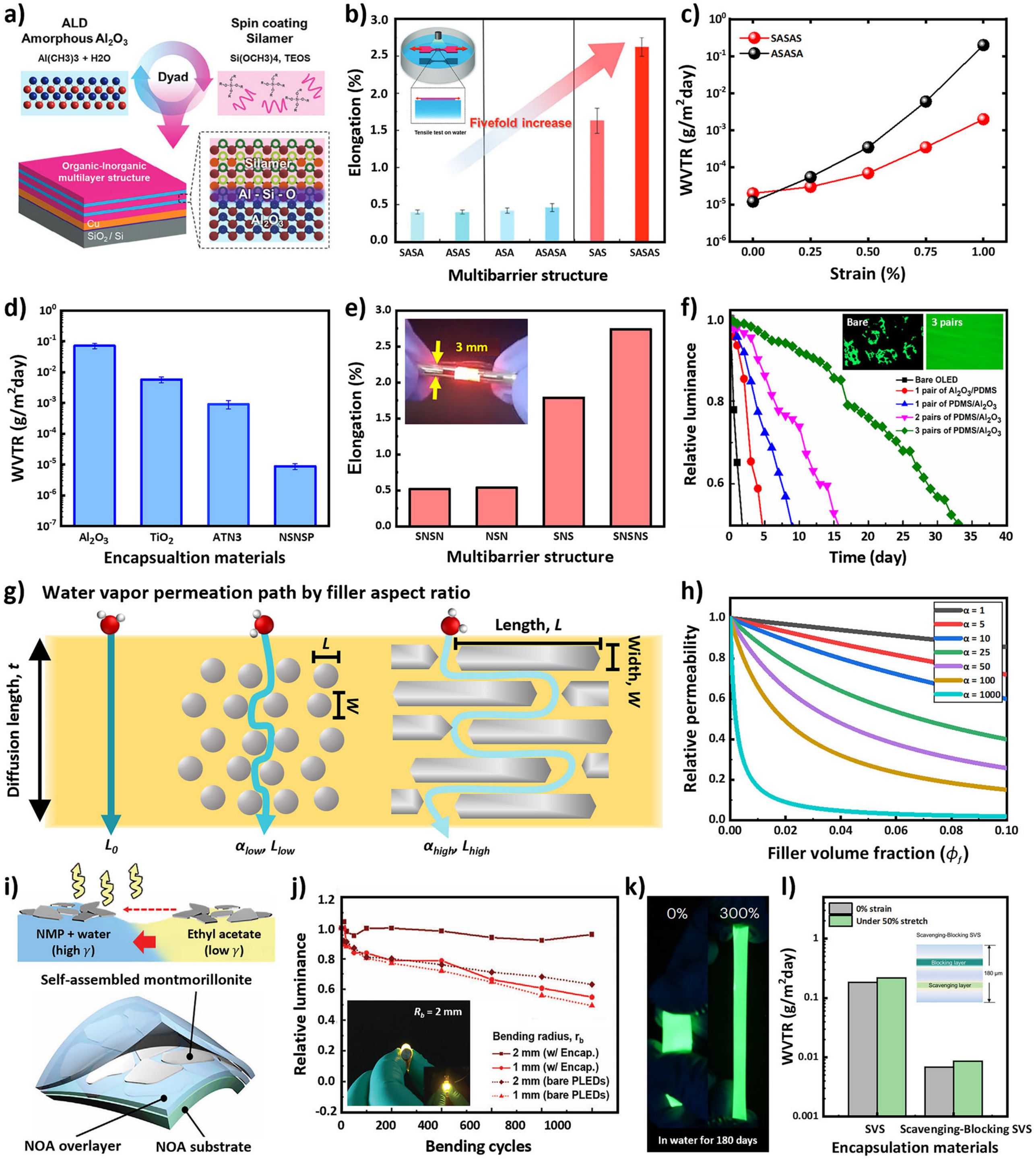

Fig. 6 | Stretchable and flexible optoelectronic devices using hybrid organic inorganic multilayer and composite encapsulation materials. **a** Schematic of Al_2O_3/silamer multilayer fabrication process. **b** Results of tensile test on various multibarrier structures (S: silamer, A: Al_2O_3). **c** Results of electrical Ca test on multibarrier structures. Adapted with permission from ref. 78. Copyright 2024, Wiley-VCH GmbH. **d** Results of electrical Ca test on Al_2O_3, TiO_2, ATN3 nanolaminate, and NSNSP. **e** Results of tensile test on SNSN, NSN, SNS, SNSNS multibarrier structures. Adapted with permission from ref. 85. Copyright 2025, The Authors. **f** Results and image of luminance measurement of OLED according to the number of dyads. Adapted with permission from ref. 48. Copyright 2023, American Chemical Society. **g** Schematic of water vapor permeation path in hybrid composite encapsulation according to impermeable filler shape. **h** Relative permeability as a function of filler volume fraction, based on the Nielsen model. Adapted from ref. 80. Available under a CC-BY 4.0 license. Copyright 2022, The Authors. **i** Schematics of fabrication of parallel-aligned montmorillonite flakes by Marangoni forces. **j** Results of mechanical reliability test on PLEDs with 3-dyad montmorillonite/NOA hybrid encapsulation during cyclic bending test. Adapted with permission from ref. 31. Copyright 2024, Wiley-VCH GmbH. **k** Photographs of SVS-encapsulated $CsPbBr_3$ quantum dots stretched to 300% after 180 days in water. **l** WVTR of the 180-μm-thick scavenging-blocking SVS under 50% strain. Adapted with permission from ref. 114. Copyright 2025, The Authors.

dense mixed interlayer not only increases the overall flexibility, but also further impedes moisture penetration. PDMS is a representative polymer substrate with a high free volume (18%), high thermal stability, and abundant surface hydroxyl groups, making it a suitable substrate for ALI-based inorganic deposition[89]. 3-dyad of ALI-deposited Al_2O_3 layers (50 nm) on PDMS (22 μm) achieved a low WVTR of 9.24×10^{-5} g/m²·day under ambient conditions[48]. Optical Ca test further revealed that, even after 50 bending cycles at a bending radius of 5 mm, the hybrid encapsulation preserved 50% of unoxidized Ca for up to 8 h. These results demonstrated its robust barrier integrity and mechanical durability under repeated deformation and prolonged lifetime in ambient conditions. When applied as a top barrier film for OLEDs, it maintained 50% of the initial luminance for 33 h, confirming its suitability for practical stretchable optoelectronic applications (Fig. 6f).

Multilayer structures can markedly enhance barrier performance by effectively prolonging the water vapor diffusion path. However, even when at thicknesses of only a few nanometers, inorganic layers with elastic modulus in $10–10^2$ GPa can substantially diminish overall flexibility. To address this mechanical constraint, composite encapsulations have been developed in which discrete inorganic fillers, rather than continuous in-plane layers, are dispersed within an organic matrix[31,50,86]. These fillers, introduced as spherical, platelet, or other morphologies, are assumed to be completely impermeable to water vapor[80]. Consequently, gas molecules cannot penetrate across the fillers and should move around them, thereby increasing the effective permeation path length as shown in Fig. 6g. The permeability, P of the gas through the composite film is defined in Eq. (8) as the product of its diffusivity, D and solubility, S within the organic matrix:

$$P = D \cdot S. \tag{8}$$

Depending on the volume fraction of filler, ϕ_f and morphology of the impermeable fillers, the diffusivity and solubility terms can be redefined as Eqs. (9) and (10):

$$D = \frac{D_0}{\tau}. \tag{9}$$

$$S = S_0 \cdot \left(1 - \phi_f\right), \tag{10}$$

where D_0 and S_0 are the gas diffusivity and solubility in a pure organic matrix, respectively, and τ is the tortuosity factor, defined as the travel distance of a gas molecule relative to the total film thickness. Therefore, the total permeability and relative permeability are expressed in Eqs. (11) and (12):

$$P = D \cdot S = \frac{D_0}{\tau} \cdot S_0 \cdot \left(1 - \phi_f\right), \tag{11}$$

$$\frac{P}{P_0} = \frac{D \cdot S}{D_0 \cdot S_0} = \frac{\left(1 - \phi_f\right)}{\tau}. \tag{12}$$

These relationships represent the general form used in filler-based encapsulation models, where impermeable fillers both limit the available diffusion area and increase the tortuosity of the permeation path. The travel distance of a gas molecule is strongly influenced by the filler geometry, which can be categorized into spherical particles (e.g., SiO_2, ZnO) and high-aspect-ratio platelets (e.g., SiO_2 flakes, graphene oxide nanosheets). For the case of dilute dispersions of spherical fillers in a polymer matrix ($\phi_f < 0.2$), the Maxwell model describes the relative permeability according to Eq. (13)[110]:

$$\frac{P}{P_0} = \frac{\left(1 - \phi_f\right)}{\left(1 + \frac{\phi_f}{2}\right)}, \tag{13}$$

since the numerator corresponds to the τ in Eq. (12), τ from the Maxwell model can be expressed as:

$$\tau = 1 + \frac{\phi_f}{2} \tag{14}$$

Nielsen model describes the rectangular filler geometries, when the fillers are evenly, regularly, and dilute dispersed ($\phi_f \leq 0.1$), the relative permeability and tortuosity factors are expressed by Eqs. (15) and (16)[111]:

$$\frac{P}{P_0} = \frac{\left(1 - \phi_f\right)}{\left(1 + \frac{L}{2W} \cdot \phi_f\right)}, \tag{15}$$

$$\tau = 1 + \frac{L}{2W} \cdot \phi_f, \tag{16}$$

where L and W denote the length and width of the filler, respectively, and the aspect ratio, α, is defined as L/W. Analysis of Eq. (15) indicates that the reduction in relative permeability becomes markedly steeper with increasing α, as shown in Fig. 6h[80]. At higher α values, even a small increase in ϕ_f leads to a pronounced extension of the gas diffusion path. In other words, as α increases, the detour length of gas molecules becomes longer, thereby delaying the arrival of water molecules capable of oxidizing the organic components beneath the encapsulation. In practice, when fillers with $\alpha \geq 1000$ are employed, adding as little as 2% of ϕ_f can reduce permeability by more than 90%. This highlights the advantage of achieving high impermeability with only a small filler loading, thereby largely preserving the intrinsic stretchability of the organic matrix. The orientation of the fillers relative to the direction of water vapor penetration also exerts a substantial influence on permeability. The Bharadwaj model introduces an orientation factor, S', and modifies the tortuosity factor τ derived from the Nielsen model, as expressed in Eqs. (17) and (18)[112]:

$$S' = \frac{1}{2} \cdot <3\cos^2\theta - 1>, (-0.5 < S' < 1) \tag{17}$$

$$\tau = 1 + \frac{L}{2W} \cdot \phi_d \cdot \frac{2}{3} \cdot \left(S' + \frac{1}{2}\right), \tag{18}$$

where θ denotes the angle between the filler and the longitudinal direction of the film. When water vapor penetrates through the thickness direction, θ= 0° corresponds to fillers oriented horizontally, effectively blocking vapor penetration, leading S'=1. Conversely, θ=90° corresponds to fillers aligned vertically, providing minimal obstruction to gas transport, resulting in S'=−0.5. The tortuosity factor defined as Eq. (11), the relative permeability can be expressed as Eq. (19):

$$\frac{P}{P_0} = \frac{\left(1 - \phi_f\right)}{\left(1 + \frac{L}{2W} \cdot \phi_d \cdot \frac{2}{3} \cdot \left(S' + \frac{1}{2}\right)\right)}. \tag{19}$$

Beyond the shape, aspect ratio, and orientation of fillers, several additional factors also influence the barrier performance of filler-based composites. These include variations in filler geometry (e.g., tubular or cylindrical forms), the slit dimensions between adjacent fillers, and the degree of filler packing[80]. According to various mathematical models, it is possible to achieve simultaneous optimization of impermeability and stretchability while preserving the intrinsic mechanical compliance of the organic matrix.

According to Eq. (12), aligning two-dimensional (2D) flakes to the longitudinal direction of the encapsulation layer ($S' \approx 1$) minimizes the gas permeability. However, achieving such ideal alignment in hybrid composites remains a critical processing challenge. To address this, a co-solvent-assisted method has been demonstrated, inducing highly parallel alignment of 2D montmorillonite flakes by maximizing the Marangoni force, as illustrated in Fig. 6i[31]. Montmorillonite is a clay mineral consisting of one octahedral alumina crystal sheet sandwiched between two tetrahedral silica sheets and has been widely applied as an impermeable filler in hybrid encapsulation due to their high transparency and flexibility. Using this method, a 3-dyad of PUA/montmorillonite hybrid encapsulation exhibited a predicted WVTR of 2.42×10^{-3} g/m²·day at ambient condition due to the uniformly aligned flakes. Long-term stability and mechanical reliability tests on polymer solar cell (PSC) and polymer LED (PLED) devices demonstrated 90% retention of the initial PCE after 1000 h and 96% luminance retention even after 1000 bending cycles at a 2 mm of bending radius, respectively (Fig. 6j). Improving barrier performance through filler alignment at the cell scale is critical, but ensuring stability at the module scale presents additional challenges. In solar cell technologies, evaluating the operational reliability of modules—beyond the single-cell level—is essential for commercialization. Perovskite solar modules (PSMs), with active areas an order of magnitude larger than individual cells, are particularly vulnerable to degradation from moisture penetration, mechanical stress, and thermal effects induced by electrical operation. To mitigate these issues, a hybrid encapsulation strategy was developed by incorporating hexagonal boron nitride (h-BN) nanosheets into a polyisobutylene (PIB) matrix[113]. Owing to their high thermal conductivity (>700 W/mK) in monolayer form, h-BN flakes served both as impermeable barriers and as heat-dissipating elements, thereby enhancing thermal stability. The resulting PIB:h-BN encapsulation achieved a WVTR of 2×10^{-5} g/m²·day and enabled PSMs to retain over 80% of their initial PCE after 1000 h of damp-heat testing at 85 °C (ISOS-D-2). These findings demonstrate that integrating thermally conductive fillers can simultaneously improve barrier performance and thermal management, offering a viable pathway toward achieving reliable module-scale stability.

Recent advances have demonstrated a hybrid sealing platform that simultaneously achieves rubber-like stretchability and aluminum-foil-level impermeability[114]. The key design principle involves engineering a viscoplastic surface on a SIBS elastomer, in which maleic anhydride-grafted polypropylene (MAPP) microdomains are selectively localized near the surface through controlled phase separation. This near-surface viscoplastic layer forms intimate, nearly defect-free contact with the device, suppressing side-leakage pathways while the bulk matrix remains elastic. As shown in Fig. 6k, SVS-sealed $CsPbBr_3$ quantum dot samples retained bright green emission even when stretched to 300% after 180 days of immersion in water. To further mitigate bulk water penetration, a scavenging layer consisting of 3 Å molecular sieves and a high-viscosity glycerol/ectoine liquid was inserted between two SVS layers. This architecture exhibits a WVTR below the MOCON detection limit of 9×10^{-5} g/m²·day at 25 °C/90% RH, and this value remains unchanged even after 50,000 stretching cycles at 100% strain—demonstrating exceptional mechanical durability and moisture-blocking capability. The SVS platform can also integrate a metal-like gas barrier by incorporating a conformal eutectic gallium–indium (EGaIn) liquid metal layer as a blocking layer. This configuration enables multilayer architectures that combine scavenging and blocking functionalities while providing high poke resistance and mechanical robustness without introducing interfacial defects. As shown in Fig. 6l, a five-layer scavenging–blocking SVS film maintains a WVTR on the order of 10^{-3} g/m²·day even at 50% strain.

Liquid metals (LMs) such as EGaIn have been widely explored as stretchable electrodes, and recent studies have extended their use to stretchable encapsulation. Benefiting from their nearly zero effective elastic modulus and fluidic deformability, LMs can sustain virtually unlimited strain while retaining metal-like gas barrier performance[115,116]. Because LMs remain in the liquid phase, a soft elastomeric reservoir (e.g., PDMS) is typically used to confine the LM, often with glass-bead spacers to prevent reservoir-surface contact and mechanical failure during large deformations such as stretching or twisting, thereby preserving device function[117]. However, the intrinsic optical opacity of metals limits their applicability as top encapsulation layers for optoelectronic devices, where high optical transmittance is required. Consequently, LM-based encapsulation has primarily been demonstrated in non-optical systems including wearable strain sensors and organic-electrolyte lithium-ion batteries (LIBs)[118]. Recent work has attempted to mitigate this limitation by leveraging the defect-free sealing behavior of liquids—for example, by infiltrating transparent lubricant oils into silicone elastomers to realize optically transparent and stretchable encapsulation layers[119,120].

Beyond material- and structure-specific advances, the heterogeneous nature of hybrid systems inevitably introduces distinct failure mechanisms under mechanical deformation. The first failure mode arises from the brittleness of inorganic layers. Owing to their high elastic modulus and low fracture strain, tensile deformation above a critical threshold induces channel cracking through the full film thickness. When the stress intensity factor (SIF) at the crack tip remains high, cracks propagate unstably and form periodic channel-crack arrays[78]. These continuous cracks create direct permeation pathways from the surface to the substrate, accelerating moisture and oxygen ingress. Under cyclic loading, crack opening and crack length further increase, which may eventually initiate delamination. In contrast, multilayer architectures in which organic layers are inserted between inorganic sublayers can mitigate this failure. The organic layers absorb deformation energy and reduce interfacial stress concentration, thereby lowering the energy release rate at the crack tip. Cracks in the inorganic layers are therefore impeded or deflected at the interfaces rather than propagating through the entire encapsulation stack. Continuous channel cracking is effectively suppressed, and the applied strain is dissipated through microcrack formation within individual inorganic layers[78,121]. As microcrack density increases, the SIF at each crack decreases, leading to saturation of crack opening and length, which stabilizes propagation and improves overall elongation.

A second failure mode arises from mechanical and interfacial mismatch between organic and inorganic components. In hybrid composites incorporating highly impermeable fillers such as silica nanoparticles within an organic matrix, large tensile or cyclic deformation can induce stress concentration at the organic–inorganic interface, leading to interfacial separation and degradation of barrier performance. When interfacial adhesion is sufficiently strong, repeated tensile or bending deformation imposes excessive stress on brittle fillers, causing fracture within the inorganic phase and thereby accelerating moisture ingress. In multilayer architectures, in-plane iso-strain loading can induce cracks perpendicular to the stretching direction within inorganic sublayers; these cracks may serve as rapid permeation pathways or initiate interfacial delamination. Additional mismatches, such as differences in Poisson's ratio leading to unequal lateral contraction, or differences in coefficient of thermal expansion (CTE) causing thermally induced interfacial stresses, also contribute to mechanical failure. Furthermore, moisture-induced swelling of organic layers can promote layer-by-layer delamination, accelerating encapsulation degradation well before the intended device lifetime. These failure mechanisms underscore the necessity of minimizing property mismatches through careful selection of organic and inorganic layers, engineering interfacial adhesion via interlayers, and optimizing deposition or transfer-based fabrication methods to achieve mechanically robust hybrid encapsulation structures.

Structural approaches to stretchable encapsulation

The pre-stretch method has been proposed as an effective encapsulation strategy for stretchable devices, enabling simultaneous improvements in mechanical stretchability and operational stability. As illustrated in Fig. 7a, the device is first subjected to a defined pre-strain, after which an encapsulation layer is deposited. Upon release of the applied strain, the

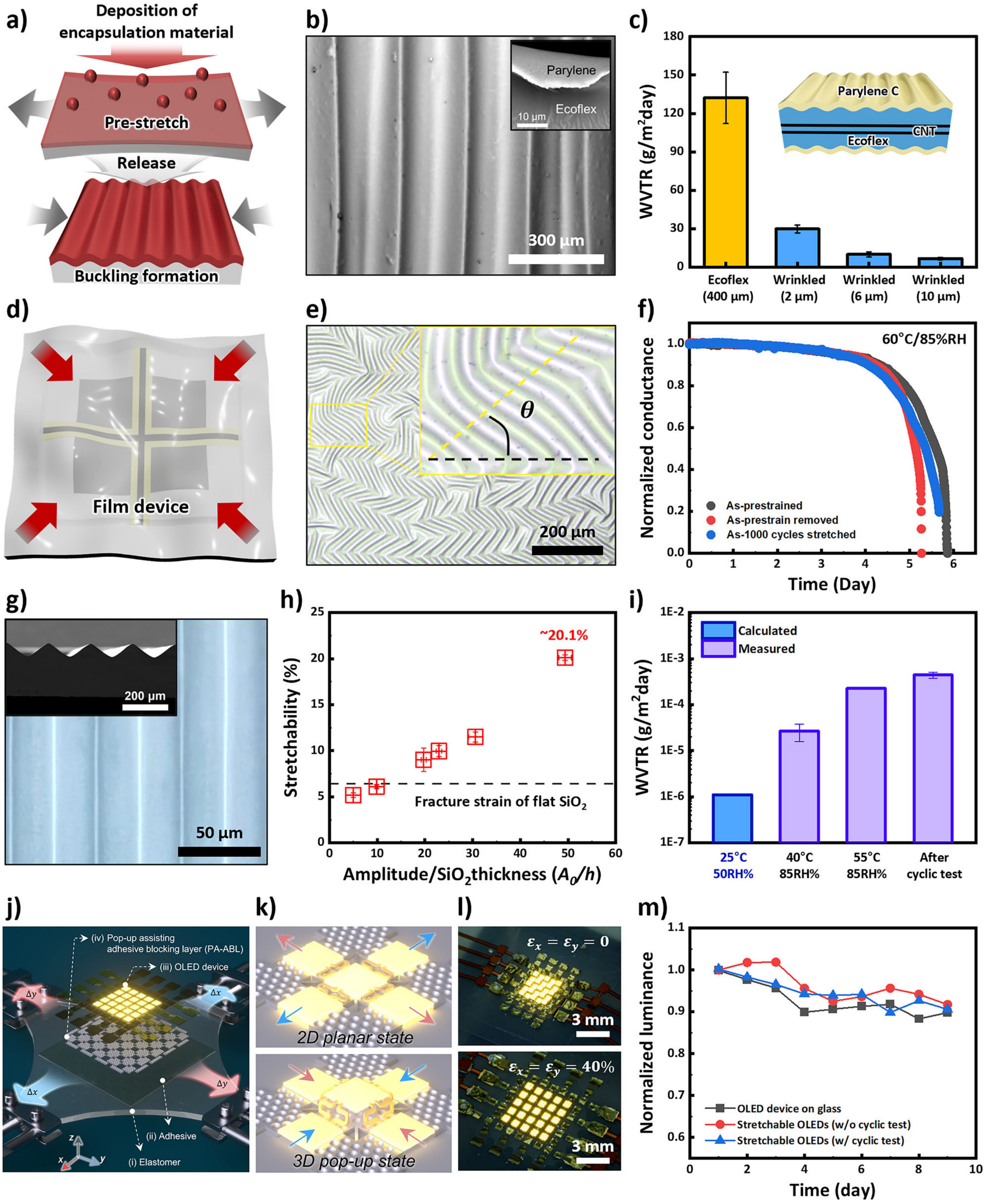

Fig. 7 | Structure-assisted encapsulation materials for enhanced stretchability. **a** Schematic of the pre-stretch method for generating a buckling-structured film. **b** SEM image of the wrinkled surface of the parylene C encapsulation layer. **c** WVTR as a function of thickness for wrinkled parylene C encapsulation layers. Adapted with permission from ref. 43. Copyright 2025, American Chemical Society. **d** Schematic of multiaxial deformation in film devices. **e** OM images of random wrinkle structures in thermally grown SiO_2. **f** Normalized conductance–time graph measured before and after 1000 cycles in wrinkle-structured thermally grown SiO_2. Adapted with permission from ref. 21. Copyright 2021, Acta Materialia Inc. Published by Elsevier Ltd. **g** OM and SEM images of uniform wavy-structures in thermally grown SiO_2. **h** Stretchability-A_0/H curve, and **i** WVTR of wavy-structured thermally grown SiO_2. Adapted with permission from ref. 22. Copyright 2023, The Authors. Advanced Electronic Materials published by Wiley-VCH GmbH. **j** Schematic illustration of the assembly strategy using PA-ABL with an OLED device on an elastomeric substrate. **k** Schematic of transition from the 2D planar state to the 3D pop-up state. **l** Photographs of a stretchable OLED device under equal biaxial strain of 0% and 40%. **m** Luminance–time curves of stretchable OLEDs. Adapted with permission from ref. 49. Copyright 2024, The Authors.

encapsulation forms periodic buckled structures. This structural modulation allows the encapsulation to deform more readily under subsequent mechanical loading, thereby enhancing the overall stretchability of the device. Depending on the mechanical properties of the thin film and its underlying substrate, buckling can manifest in various morphologies, including wrinkles, creases, and delaminated buckles[25,122]. Among these, wrinkle patterns are particularly advantageous, as they can uniformly relieve compressive stresses induced during pre-straining. Consequently, several studies have investigated the controlled formation of wrinkled structures in encapsulation layers to improve mechanical durability under cyclic deformation[43,123].

For effective wrinkle formation, the substrate–encapsulation system must support stable application of pre-strain without compromising adhesion or mechanical integrity. Silicone elastomers with high elasticity are commonly employed as substrates to meet these requirements. In one example, a carbon nanotube (CNT)-embedded Ecoflex strain sensor was pre-stretched to 120% and subsequently coated with parylene C encapsulation layers of 2, 6, and 10 μm thickness[43]. Uniform wrinkles formed in the parylene C films (Fig. 7b), preserving their intrinsic barrier properties while enhancing stretchability through gradual wrinkle unfolding. The maximum stretchability decreased with increasing parylene C thickness, from 65% to 20% and 4% for 2, 6, and 10 μm films, respectively. Post-deposition annealing produced finer and denser wrinkle morphologies, which substantially improved the stretchability of the 10 μm film from 4% to 33%. As shown in Fig. 7c, WVTR measurements under 36–38 °C/75–80% RH revealed that reducing parylene C thickness and incorporating the encapsulation layer decreased WVTR by more than fourfold compared with bare Ecoflex. Collectively, these results demonstrate that pre-strain-induced wrinkle structures can simultaneously enhance stretchability and maintain low WVTR, providing a viable pathway for encapsulation in deformable electronic systems.

For stretchable optoelectronics intended for integration with human skin, it is essential to accommodate not only uniaxial but also multiaxial deformations (Fig. 7d). This requirement has motivated the development of random buckled structures through multiaxial pre-stretching. Reported approaches include transferring thermally oxidized SiO_2 layers or thermally evaporated NOA63 films onto elastomer substrates under multiaxial pre-strain, followed by release of the applied strain to induce random wrinkle formation[21,124]. In contrast to uniaxial wrinkles, multiaxial wrinkle structures exhibit more complex morphologies that cannot be classified by mechanical properties alone, reflecting the inherent complexity of multiaxial deformation modes.

Under biaxial pre-stretch conditions, the characteristics of wrinkle structures were shown to depend on the area size[21]. Random wrinkle patterns were predominantly generated in larger regions (1 mm × 1 mm), while unidirectional wrinkle structures were mainly observed in smaller regions (100 μm × 100 μm), as shown in Fig. 7e. Stretchability was evaluated using the amplitude-to-wavelength ratio (A/λ), where amplitude (A) corresponds to half the wrinkle height and wavelength (λ) refers to the length of a single wave. These results indicate that a larger A/λ ratio is associated with an increased deformable wrinkle size, which in turn contributes to enhanced stretchability. Uniform wrinkle distribution in smaller areas provided higher stretchability, while the occurrence of triple junctions in randomly wrinkled large areas induced local stress concentration, thereby reducing the overall stretchability. Nevertheless, WVTR values, as derived from the conductance-time analysis in Fig. 7f, were 3.3×10^{-4} and 2.8×10^{-4} g/m²·day before and after 1000 cyclic stretching cycles under accelerated conditions (60 °C/85% RH), indicating negligible degradation in performance. This confirms that random buckled structures can simultaneously ensure high stretchability and stable barrier performance by maintaining low water vapor permeability under cyclic deformation. However, pre-stretch-based wrinkle structures, which are generated by compressive stress applied during fabrication, are advantageous under tensile deformation but exhibit limitations under compressive deformation. Furthermore, the non-uniformity of the wrinkle structures may lead to localized stress concentration, which could potentially degrade the mechanical reliability of the encapsulation layer. To mitigate this issue, uniform wavy structures have been proposed, which can effectively respond to both tensile and compressive deformation under free-strain conditions, thereby enhancing the mechanical stretchability of the encapsulation layer.

A wavy-structured thermally grown SiO_2 film was fabricated by forming uniaxially wave-textured patterns on a single-crystalline Si substrate through etching, followed by a high temperature oxidation process, as observed in Fig. 7g[22]. Tensile tests conducted on SiO_2 films with thicknesses of 200, 500, and 1000 nm yielded an elastic modulus of 69.01 GPa, a fracture strength of 4.42 GPa, and an elastic deformation limit of 6.58%, independent of thickness. These results indicate that the SiO_2 films were well-formed and essentially free of crystal defects. As shown in Fig. 7h, the stretchability, evaluated by varying amplitude (A_0) and film thickness (h), exhibited a clear dependence on the A_0/h ratio, with a maximum value of 20.1%. Furthermore, optical microscopy revealed no evidence of surface crack formation after 1000 stretching cycles under 10% tensile strain. As shown in Fig. 7i, to evaluate the presence of invisible defects, WVTR was measured, yielding 2.66×10^{-5} and 2.25×10^{-4} g/m²·day at 40 °C and 55 °C at 85% RH, respectively. Following cyclic deformation under 55 °C and 85% RH, the WVTR increased nearly twofold to 4.41×10^{-4} g/m²·day, thereby indicating the influence of such defects. Accordingly, the WVTR was estimated at 1.11×10^{-6} g/m²·day at 25 °C/55% RH. Even with partial performance degradation under high-temperature, high-humidity, and cyclic deformation conditions, the wavy-structured SiO_2 film exhibited high mechanical reliability and low moisture permeability, demonstrating its potential as an inorganic encapsulation material.

A 3-dyad wavy Al_2O_3/acrylic hybrid encapsulation was fabricated via a pressing process, in which wavy PDMS was pressed against the acrylic layer to form the wavy pattern, followed by Al_2O_3 deposition[123]. Wavy PDMS is generated by pre-stretching followed by Ar-plasma surface stiffening; subsequent strain release induces buckling driven by the mismatch between the rigid surface and the soft PDMS matrix. The period and amplitude of the wavy pattern can be controlled by varying the condition of plasma treatment. On this basis, bending tests revealed that shorter periods and greater amplitudes reduced maximum bending stress, thereby alleviating stress concentration during bending. WVTR measurements at 25 °C/40% RH following 200 bending cycles revealed that the planar Al_2O_3 encapsulation layer exhibited 3×10^{-4} g/m²·day, whereas the wrinkle structure reduced WVTR to 10^{-4} g/m²·day, representing a threefold improvement. These findings indicate that wavy structures ensure long-term barrier performance (low WVTR) under prolonged bending, establishing an effective design strategy to minimize deformation-induced damage in hybrid encapsulation layers susceptible to mechanical deformation.

Given that the maximum strain achievable through inorganic encapsulation structure design is inherently limited, interconnector design has been introduced as a complementary strategy to enhance the overall stretchability of devices[49,125–127]. This strategy provides mechanical stability by mitigating direct deformation of the encapsulation layer, while the buckling of the interconnector disperses strain, ultimately enhancing the overall stretchability of the device. Serpentine interconnectors and 2D rigid island array structures are effective in minimizing deformation in rigid OLED regions[125–127]; however, they are constrained by a trade-off, in which enhancing the strain capacity of the interconnectors leads to a reduction in the planar density of active components.

To overcome this limitation, a three-dimensional (3D) pop-up structure was developed by incorporating a selectively adhesive blocking layer (pA-ABL) and dual serpentine interconnectors, which enabled high stretchability while preserving high EL performance[49]. Figure 7j schematically shows the fabrication of stretchable OLEDs. The structure was realized through biaxial pre-stretching of the elastomer, onto which the grid-patterned pA-ABL and OLED layers were transferred, followed by relaxation of the pre-strain. As a result, out-of-plane buckling of the dual serpentine interconnectors and 3D pop-up deformation of the rigid islands occurred, which is schematically illustrated in Fig. 7k. Since OLEDs require

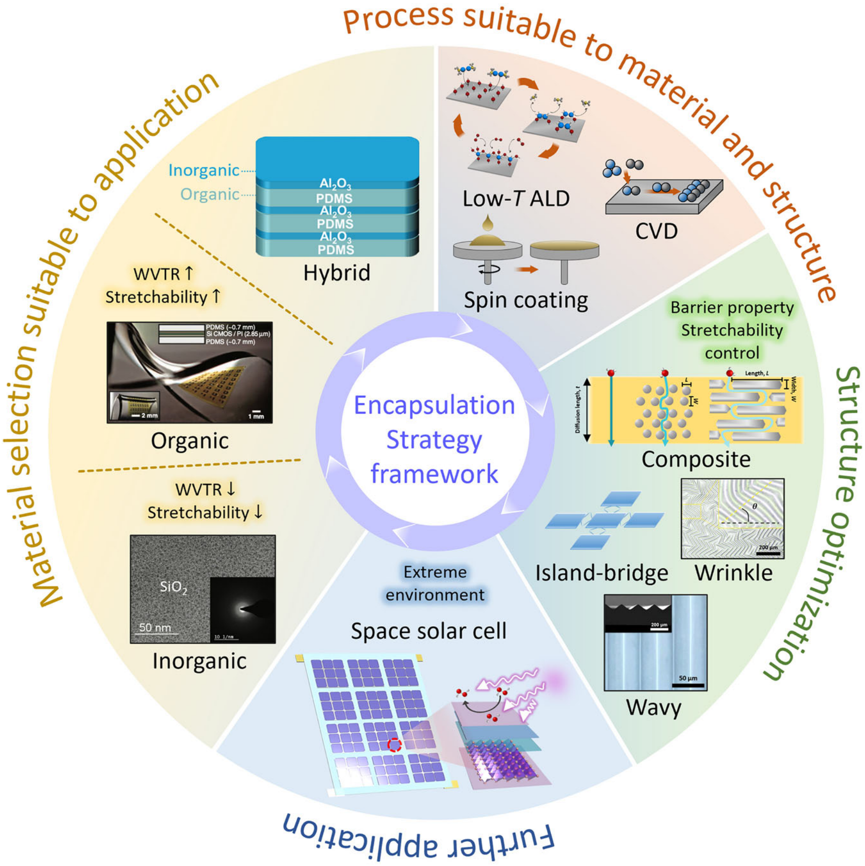

Fig. 8 | Integrated design framework for stretchable and flexible encapsulation materials. Application requirements guide the selection of organic, inorganic, and hybrid materials. Processing routes are chosen to match material constraints, while structural strategies enhance deformability and defect tolerance. These coupled choices define the pathway toward reliable encapsulation with low WVTR and high stretchability for next-generation deformable devices. Adapted with permission from refs. 21,22,47,48,55,58.

only minimal stretchability, a pV3D3/Al_2O_3/pV3D3 hybrid encapsulation, composed of alternately laminated inorganic Al_2O_3 and organic poly(1,3,5-trimethyl-1,3,5-trivinyl cyclotrisiloxane) (pV3D3), has been utilized to achieve low WVTR and high mechanical durability. As observed in Fig. 7l, implementation of the proposed structure and encapsulation in a 5 × 5 array stretchable OLED enabled system strain of up to 40%. As indicated in Fig. 7m, stretchable OLEDs exhibited long-term luminance stability provided by the encapsulation layer, comparable to that of glass-reference OLEDs, even after more than 2000 cycles of 40% biaxial strain. Accordingly, concentrating deformation in the interconnectors via buckling, while maintaining the minimally required stretchability and excellent barrier properties of the encapsulation, has been shown to enable the simultaneous realization of high stretchability and long-term stability for the device.

Structural strategies—including pre-stretch-induced wrinkle architectures, thermally oxidized wavy structures, and interconnector designs—have enabled simultaneous improvements in mechanical stretchability and long-term stability of both inorganic and organic encapsulation layers. Wrinkle and wavy structures facilitate stress relaxation during deformation, thereby preserving moisture barrier properties, while interconnector designs effectively redistribute local strain to enhance device reliability. These findings highlight that, in the development of next-generation stretchable optoelectronics, structural design can be synergistically combined with the intrinsic properties of encapsulation materials to maintain impermeability while enhancing stretchability, ultimately advancing reliable and durable device operation.

Summary and future perspectives

This review has summarized recent advances in encapsulation strategies for deformable optoelectronic devices, spanning materials, processing methods, structural designs, and their interactions with application environments. To ensure reliability, encapsulation materials should be evaluated under application-relevant conditions, including WVTR measurements at operating temperature and relative humidity in combination with mechanical strain parameters such as deformation mode, uniaxial or biaxial strain, and cycle count. Since moisture remains the dominant permeant causing degradation in most OLED and PV devices, WVTR continues to serve as the primary metric of barrier performance. However, next-generation qualification should also address strain-coupled permeation and leakage at edges and interfaces. Meeting these challenges will require environment-aware encapsulation engineering within an integrated framework that aligns application requirements, material selection, structural design, and processing methods (Fig. 8), particularly for stretchable applications.

From a materials perspective, effective permeability is minimized in dense amorphous structures with low free volume and suppressed percolation, underlying the long-term stability of ultrathin inorganic films such as ALD AlO_x, SiN_x, and SiO_x. Their high elastic modulus and low fracture strain, however, constrain deformability, leading to pinhole-defect formation and micro-crack propagation under mechanical stress. Organic materials such as parylene, PI, and PDMS offer orders-of-magnitude higher stretchability and lower bending stiffness, but their high diffusivity to water vapor results in elevated WVTR and rapid deterioration. Hybrid encapsulation strategies attempt to balance these opposing features: inorganic layers provide diffusion barriers, while organic layers smooth roughness and decouple defects, increasing tortuosity. Barrier performance generally improves with increasing dyad number. Sequential infiltration processes such as ALI and filler-reinforced polymer composites with aligned high-aspect-ratio flakes offer complementary pathways to elongate diffusion routes while preserving compliance. Interfacial reliability—through adhesion promoters and optimized interfacial fracture energy—remains another decisive factor for device lifetime.

Processing strategies must be carefully matched to intrinsic material properties. Polymer-based systems require low thermal budgets to avoid softening near T_g. Hybrid structures rely on low-temperature processes such as ALD, PEALD, and plasma-enhanced CVD (PECVD), which enable precise thickness control and high conformality over structured topographies. Plasma conditions must be optimized to balance radical reactivity against potential damage from ion bombardment or hydrogen incorporation, which can embrittle oxides or generate sub-gap states in organic layers[128,129]. Initiated CVD (iCVD) and other solvent-free polymerizations can minimize swelling and crazing of underlying films. Consequently, processing should integrate statistical control of outgassing, defect formation, and cracking, aligned with the material's intrinsic stability.

Structural design further enhances encapsulation stretchability. Positioning fragile layers near the neutral plane reduces surface strain during bending. Wrinkled and wavy architectures or serpentine meshes redistribute strain and delay crack initiation, while island–bridge layouts concentrate deformation in elastomeric interconnects, protecting barriers on rigid islands[21,22,40]. Selective encapsulation has also proven effective: in micro-LED displays, encapsulating only stretchable interconnects enhances both lifetime and flexibility; in skin-integrated systems, spatially graded permeability or micro-vented overmolds reconcile the dense barriers needed for active regions with the breathability required to prevent skin maceration.

Future application environments will further diversify encapsulation requirements. In bio-integrated electronics, encapsulation must block biofluid and mobile ions (Na^+, K^+, Cl^-) over long lifetimes that include sterilization and chronic mechanical deformation[2,130,131]. Crack-tolerant laminates with low ion permeability, hydrolytic stability, bio-compatible processing, and anti-fouling surfaces will be critical. In contrast, space applications demand resistance to UV and γ-radiation, atomic oxygen, vacuum outgassing, and extreme thermal cycling[132,133]. Encapsulation for PVs and optical systems in space must combine radiation shielding and atomic oxygen resistance with optical transparency, while minimizing microcracking from CTE mismatch. For such future applications, encapsulation will be evaluated not only by WVTR and stretchability but also under coupled conditions of strain, humidity, temperature cycling, UV/blue exposure, sweat, and biofluid immersion.

Ultimately, the strategic development of encapsulation materials will depend on quantitatively defined environmental and mechanical requirements. Material properties must be optimized to meet WVTR and optical targets; processing routes must respect thermal and solvent tolerances; and structural architectures must enhance compliance while preserving impermeability. For bio-interfaces, ion-blocking hybrids fabricated at gentle thermal budgets are expected to dominate, whereas in space, radiation-tolerant, optically clear laminates will be pivotal. The future of encapsulation will be shaped by coherent integration of materials, processes, and structures, where performance, comfort, and reliability are co-designed rather than traded off. Continued innovation is anticipated to improve quality of life, enable new device form factors, and expand the operating envelope of stretchable electronic systems.

Received: 18 September 2025; Accepted: 31 January 2026;

References

1. Lee, J.-W. et al. Dual-layered percolative networks of photoactive materials and elastomers for highly-stretchable, efficient organic photovoltaics with strain-induced power enhancement up to 60% strain. *Energy Environ. Sci.* **18**, 7089–7102 (2025).
2. Kim, D. C., Choi, M. K., Kim, D.-H. & Yang, J. Rise of intrinsically stretchable electroluminescent materials: toward free-form displays. *NPJ Flex. Electron.* **9**, 50 (2025).
3. Kim, K. et al. Intrinsically-stretchable and patternable quantum dot color conversion layers for stretchable displays in robotic skin and wearable electronics. *Adv. Mater.* **37**, e2420633 (2025).
4. Kim, D. C. et al. Intrinsically stretchable quantum dot light-emitting diodes. *Nat. Electron.* **7**, 365–374 (2024).
5. Lee, J.-W. et al. Simultaneous integration of poly(dimethylsiloxane) elastomer in polymer donor and dimer acceptor enables strain-induced power enhancement in intrinsically-stretchable organic photovoltaics. *Energy Environ. Sci.* **18**, 3325–3340 (2025).
6. Kim, H. et al. Integrated stretchable displays with integrated pixel density via overlapped pixels. *NPJ Flex. Electron.* **9**, 91 (2025).
7. Chun, F. et al. Multicolour stretchable perovskite electroluminescent devices for user-interactive displays. *Nat. Photon.* **18**, 856–863 (2024).
8. Lee, S. et al. Advancing high-efficiency, stretchable organic solar cells: novel liquid metal electrode architecture. *Energy Environ. Sci.* **17**, 8915–8925 (2024).
9. Jeon, H. et al. Nanomechanical insights into enhancing flexibility and reliability in deformable optoelectronic devices. *ACS Appl. Mater. Interfaces* **17**, 42568–42585 (2025).
10. Park, T. et al. Advances in flexible, foldable, and stretchable quantum dot light-emitting diodes: materials and fabrication strategies. *Korean J. Chem. Eng.* **41**, 3517–3543 (2024).
11. Xu, H. et al. A fully integrated, standalone stretchable device platform with in-sensor adaptive machine learning for rehabilitation. *Nat. Commun.* **14**, 7769 (2023).
12. Hwang, G. S. et al. Highly elastic and conductive metallic interconnect with crystalline-amorphous nanolaminate. *ACS Appl. Mater. Interfaces* **15**, 15863–15871 (2023).
13. Lee, J. W. et al. Intrinsically-stretchable, efficient organic solar cells achieved by high-molecular-weight, electro-active polymer acceptor additives. *Adv. Energy Mater.* **12**, 2200887 (2022).
14. Yokota, T. et al. Ultraflexible organic photonic skin. *Sci. Adv.* **2**, e1501856 (2016).
15. Lee, J. et al. Visual complexity of head-up display in automobiles modulates attentional tunneling. *Hum. Factors* **66**, 1879–1892 (2024).
16. Lv, Z., Xu, Y., Yang, Y. & Liu, J. Multiplane holographic augmented reality head-up display with a real-virtual dual mode and large eyebox. *Appl. Opt.* **61**, 9962–9971 (2022).
17. Shi, X. et al. Large-area display textiles integrated with functional systems. *Nature* **591**, 240–245 (2021).
18. Angmo, D. et al. Toward rollable printed perovskite solar cells for deployment in low-Earth orbit space applications. *ACS Appl. Energy Mater.* **7**, 1777–1791 (2024).
19. VanSant, K. T. et al. Combined stress testing of perovskite solar cells for stable operation in space. *ACS Appl. Energy Mater.* **6**, 10319–10326 (2023).
20. Nam, M. et al. Highly reliable and stretchable OLEDs based on facile patterning method: toward stretchable organic optoelectronic devices. *npj Flex. Electron.* **8**, 17 (2024).
21. Kim, N.-H. et al. Enhanced biaxial stretchability of wrinkled SiO_2 thin films for stretchable encapsulation. *Scr. Mater.* **207**, 114280 (2022).
22. Kim, H., Hwang, G. S., Lee, S. & Kim, J. Y. Enhanced stretchability of wavy-structured thermally grown silicon dioxide films for stretchable encapsulation. *Adv. Electron. Mater.* **9**, 2300078 (2023).
23. Deng, Y. et al. Rotating square tessellations enabled stretchable and adaptive curved display. *NPJ Flex. Electron.* **8**, 4 (2024).
24. Jo, M. et al. 3D printer-based encapsulated origami electronics for extreme system stretchability and high areal coverage. *ACS Nano* **13**, 12500–12510 (2019).
25. Wang, Q. & Zhao, X. A three-dimensional phase diagram of growth-induced surface instabilities. *Sci. Rep.* **5**, 8887 (2015).
26. Fan, X. et al. PEDOT:PSS for flexible and stretchable electronics: modifications, strategies, and applications. *Adv. Sci.* **6**, 1900813 (2019).
27. Liang, J., Tong, K. & Pei, Q. A water-based silver-nanowire screen-print ink for the fabrication of stretchable conductors and wearable thin-film transistors. *Adv. Mater.* **28**, 5986–5996 (2016).

28. Sang, M., Kim, K., Shin, J. & Yu, K. J. Ultra-thin flexible encapsulating materials for soft bio-integrated electronics. *Adv. Sci.* **9**, e2202980 (2022).
29. Han, W. B., Hwang, S.-W. & Yeo, W.-H. Recent advances in encapsulation strategies for flexible transient electronics. *Flex. Print. Electron.* **9**, 033001 (2024).
30. Mariello, M., Kim, K., Wu, K., Lacour, S. P. & Leterrier, Y. Recent advances in encapsulation of flexible bioelectronic implants: materials, technologies, and characterization methods. *Adv. Mater.* **34**, e2201129 (2022).
31. Nam, Y. S. et al. Flexible and transparent encapsulation films with self-assembled montmorillonite induced by Marangoni forces. *Adv. Mater. Technol.* **9**, 2400452 (2024).
32. Bak, Y. et al. Highly reliable textile-based stretchable photo-heating platform: wearable OLEDs with Kirigami-patterned transferable transparent stretchable electronics. *Chem. Eng. J.* **522**, 167217 (2025).
33. Yan, B., Qin, L., Tao, S. & Fang, G. Development and challenges of large space flexible solar arrays. *SSPWT* **2**, 33–42 (2025).
34. Li, J. et al. A brief review of high efficiency III-V solar cells for space application. *Front. Phys.* **8**, 631925 (2021).
35. Jeong, E. G., Kwon, J. H., Kang, K. S., Jeong, S. Y. & Choi, K. C. A review of highly reliable flexible encapsulation technologies towards rollable and foldable OLEDs. *J. Inf. Disp.* **21**, 19–32 (2019).
36. Lewis, J. Material challenge for flexible organic devices. *Mater. Today* **9**, 38–45 (2006).
37. Shin, H. et al. Stretchable electroluminescent display enabled by graphene-based hybrid electrode. *ACS Appl. Mater. Interfaces* **11**, 14222–14228 (2019).
38. Liu, G. et al. Flexible, stretchable, and luminescent hydrogels based on a polydimethylsiloxane-coated CsPbBr3 nanostructure for elastomers. *ACS Appl. Nano Mater.* **6**, 9588–9597 (2023).
39. Kim, S. H. et al. A compact polymer–inorganic hybrid gas barrier nanolayer for flexible organic light-emitting diode displays. *npj Flex. Electron.* **6**, 21 (2022).
40. Sang, M. et al. Ultrahigh sensitive Au-doped silicon nanomembrane based wearable sensor arrays for continuous skin temperature monitoring with high precision. *Adv. Mater.* **34**, e2105865 (2022).
41. Kwon, J. I. et al. Ultrahigh-resolution full-color perovskite nanocrystal patterning for ultrathin skin-attachable displays. *Sci. Adv.* **8**, eadd0697 (2022).
42. Lee, K. et al. Highly efficient pure red light-emitting diodes through surface bromination of $CsPbI_3$ perovskite nanocrystals for skin-attachable displays. *Mater. Today* **75**, 2–10 (2024).
43. Huang, X. et al. Stretchable encapsulation for implantable strain sensors. *ACS Appl. Mater. Interfaces* **17**, 41015–41027 (2025).
44. Zhou, T. et al. 3D printable high-performance conducting polymer hydrogel for all-hydrogel bioelectronic interfaces. *Nat. Mater.* **22**, 895–902 (2023).
45. Woo, J. H. et al. Amorphous alumina film robust under cyclic deformation: a highly impermeable and a highly flexible encapsulation material. *ACS Appl. Mater. Interfaces* **13**, 46894–46901 (2021).
46. Oh, S. J. et al. Nanolaminate-induced mechanically and environmentally robust Al_2O_3/TiO_2 thin film encapsulation by low-temperature atomic layer deposition: toward flexible and wearable OLEDs. *Adv. Mater. Technol.* **9**, 2400381 (2024).
47. Kim, S.-H. et al. Highly impermeable and flexible silica encapsulation films synthesized by sol–gel process. *Nano Res.* **15**, 7476–7483 (2022).
48. Weng, Y. et al. Design and fabrication of $PDMS/Al_2O_3$ hybrid flexible thin films for OLED encapsulation applications. *ACS Appl. Polym. Mater.* **5**, 10148–10157 (2023).
49. Kim, S. B. et al. 3D height-alternant island arrays for stretchable OLEDs with high active area ratio and maximum strain. *Nat. Commun.* **15**, 7802 (2024).
50. Ko, G. J. et al. Materials and designs for extremely efficient encapsulation of soft, biodegradable electronics. *Adv. Funct. Mater.* **34**, 2403427 (2024).
51. Yoo, H., Lee, S.-H., Kim, S.-M., Jo, J.-H. & Kim, J.-Y. Research progress in flexible and stretchable encapsulation materials for electronics. *J. Flex. Print. Electron.* **4**, 15–30 (2025).
52. Song, E., Li, J. & Rogers, J. A. Barrier materials for flexible bioelectronic implants with chronic stability—current approaches and future directions. *APL Mater.* **7**, 050902 (2019).
53. Cho, M. et al. Ultra-thin thermally grown silicon dioxide nanomembrane for waterproof perovskite solar cells. *J. Power Sources* **563**, 232810 (2023).
54. Hu, Z. et al. Bioresorbable multilayer organic-inorganic films for bioelectronic systems. *Adv. Mater.* **36**, e2309421 (2024).
55. Li, H., Ma, Y. & Huang, Y. Material innovation and mechanics design for substrates and encapsulation of flexible electronics: a review. *Mater. Horiz.* **8**, 383–400 (2021).
56. Shao, Y. et al. A universal packaging substrate for mechanically stable assembly of stretchable electronics. *Nat. Commun.* **15**, 6106 (2024).
57. Wang, S. et al. Skin electronics from scalable fabrication of an intrinsically stretchable transistor array. *Nature* **555**, 83–88 (2018).
58. Kim, D.-H. et al. Stretchable and foldable silicon integrated circuits. *Science* **320**, 507–511 (2008).
59. Huang, Z. et al. Three-dimensional integrated stretchable electronics. *Nat. Electron.* **1**, 473–480 (2018).
60. Jiao, R. et al. Vertical serpentine interconnect-enabled stretchable and curved electronics. *Microsyst. Nanoeng.* **9**, 149 (2023).
61. Shangguan, L. et al. Modulating residual stress based on atomic layer deposition to enhance the adhesion of parylene C for encapsulation of flexible organic light-emitting diodes. *Appl. Phys. Express* **16**, 041004 (2023).
62. Nam, K.-H., Seo, K., Seo, J., Khan, S. B. & Han, H. Ultraviolet-curable polyurethane acrylate nanocomposite coatings based on surface-modified calcium carbonate. *Prog. Org. Coat.* **85**, 22–30 (2015).
63. Zhang, Z. et al. High-brightness all-polymer stretchable LED with charge-trapping dilution. *Nature* **603**, 624–630 (2022).
64. Song, K.-Y., Zhang, H., Zhang, W.-J. & Teixeira, A. Enhancement of the surface free energy of PDMS for reversible and leakage-free bonding of PDMS–PS microfluidic cell-culture systems. *Microfluid. Nanofluid.* **22**, 135 (2018).
65. Jinno, H. et al. Stretchable and waterproof elastomer-coated organic photovoltaics for washable electronic textile applications. *Nat. Energy* **2**, 780–785 (2017).
66. Kaltenbrunner, M. et al. Flexible high power-per-weight perovskite solar cells with chromium oxide-metal contacts for improved stability in air. *Nat. Mater.* **14**, 1032–1039 (2015).
67. Bertrand, J. A. & George, S. M. Evaluating Al_2O_3 gas diffusion barriers grown directly on Ca films using atomic layer deposition techniques. *J. Vac. Sci. Technol., A.* **31**, 01A122 (2013).
68. Kim, D. H. et al. Dissolvable films of silk fibroin for ultrathin conformal bio-integrated electronics. *Nat. Mater.* **9**, 511–517 (2010).
69. Nam, T. et al. A composite layer of atomic-layer-deposited Al_2O_3 and graphene for flexible moisture barrier. *Carbon* **116**, 553–561 (2017).
70. Dameron, A. A. et al. Gas diffusion barriers on polymers using multilayers fabricated by Al_2O_3 and rapid SiO_2 atomic layer deposition. *J. Phys. Chem. C.* **112**, 4573–4580 (2008).
71. Jang, D., Meza, L. R., Greer, F. & Greer, J. R. Fabrication and deformation of three-dimensional hollow ceramic nanostructures. *Nat. Mater.* **12**, 893–898 (2013).
72. Lee, L. et al. Ultra gas-proof polymer hybrid thin layer. *Nano Lett.* **18**, 5461–5466 (2018).

73. Park, S.-H. K. et al. Ultrathin film encapsulation of an OLED by ALD. *Electrochem. Solid State Lett.* **8**, 21–23 (2005).
74. Duan, Y. et al. Thin-film barrier performance of zirconium oxide using the low-temperature atomic layer deposition method. *ACS Appl. Mater. Interfaces* **6**, 3799–3804 (2014).
75. George, S. M. Atomic layer deposition: an overview. *Chem. Rev.* **110**, 111–131 (2009).
76. Kim, S. K. et al. Low Temperature (<100° C) deposition of aluminum oxide thin films by ALD with O3 as oxidant. *J. Electrochem. Soc.* **153**, 69–76 (2006).
77. Kwon, B. H. et al. Organic/inorganic hybrid thin-film encapsulation using inkjet printing and PEALD for industrial large-area process suitability and flexible OLED application. *ACS Appl. Mater. Interfaces* **13**, 55391–55402 (2021).
78. Lee, S. W. et al. Highly reliable and ultra-flexible wearable OLEDs enabled by environmentally and mechanically robust hybrid multibarrier encapsulation layers. *Adv. Funct. Mater.* **35**, 2411802 (2024).
79. Park, Y. C. et al. A highly bendable thin film encapsulation by the modulation of thermally induced interfacial residual stress. *Appl. Surf. Sci.* **598**, 153874 (2022).
80. Idris, A., Muntean, A. & Mesic, B. A review on predictive tortuosity models for composite films in gas barrier applications. *J. Coat. Technol. Res.* **19**, 699–716 (2022).
81. Wang, H. et al. Hermetic seal for perovskite solar cells: An improved plasma enhanced atomic layer deposition encapsulation. *Nano Energy* **69**, 104375 (2020).
82. Keum, C. et al. A substrateless, flexible, and water-resistant organic light-emitting diode. *Nat. Commun.* **11**, 6250 (2020).
83. Kang, K. S., Jeong, S. Y., Jeon, Y., Kwon, J. H. & Choi, K. C. Enhancing flexibility and reliability in wearable OLEDs through silbione-blended hybrimer-based encapsulation. *NPJ Flex. Electron.* **9**, 49 (2025).
84. Son, Y. H. et al. Highly reliable organic light-emitting diodes with optimized fill factor based on rotational membrane design for stretchable displays. *Mater. Horiz.* **12**, 7580–7593 (2025).
85. Kwon, J. H. et al. Highly efficient, reliable, and ultraflexible bio-organic light-emitting diode patch. *NPJ Flex. Electron.* **9**, 55 (2025).
86. Huang, H.-D. et al. High barrier graphene oxide nanosheet/poly(vinyl alcohol) nanocomposite films. *J. Membr. Sci.* **409–410**, 156–163 (2012).
87. Castro-Hermosa, S., Top, M., Dagar, J., Fahlteich, J. & Brown, T. M. Quantifying performance of permeation barrier—encapsulation systems for flexible and glass-based electronics and their application to perovskite solar cells. *Adv. Electron. Mater.* **5**, 1800978 (2019).
88. Chen, N. et al. Low substrate temperature encapsulation for flexible electrodes and organic photovoltaics. *Adv. Energy Mater.* **5**, 1401442 (2014).
89. Zhang, Y. et al. Stretchable PDMS encapsulation via SiO_2 Doping and atomic layer infiltration for flexible displays. *Adv. Mater. Interfaces* **9**, 2101857 (2022).
90. Nakano, Y., Yanase, T., Nagahama, T., Yoshida, H. & Shimada, T. Accurate and stable equal-pressure measurements of water vapor transmission rate reaching the 10(-6) g m(-2) day(-1) range. *Sci. Rep.* **6**, 35408 (2016).
91. Svens, P., Kjell, M., Tengstedt, C., Flodberg, G. & Lindbergh, G. Li-ion pouch cells for vehicle applications—studies of water transmission and packing materials. *Energies* **6**, 400–410 (2013).
92. Chen, Z. Y. et al. Stretchable organic light-emitting devices with invisible orderly wrinkles by using a transfer-free technique. *Adv. Mater. Technol.* **7**, 2101263 (2022).
93. Xu, S. et al. Stretchable batteries with self-similar serpentine interconnects and integrated wireless recharging systems. *Nat. Commun.* **4**, 1543 (2013).
94. Kwak, J. Y. et al. Manufacturing of stretchable substrate with biaxial strain control for highly-efficient stretchable solar cells and displays. *Sci. Rep.* **13**, 20460 (2023).
95. Mariello, M. et al. Magnesium test: universal and ultra-sensitive method for measuring reliability of thin-film-encapsulated bioelectronic implants in physiological environment. *Adv. Funct. Mater.* **34**, 2315420 (2024).
96. Jeong, E. G., Han, Y. C., Im, H.-G., Bae, B.-S. & Choi, K. C. Highly reliable hybrid nano-stratified moisture barrier for encapsulating flexible OLEDs. *Org. Electron.* **33**, 150–155 (2016).
97. Li, C. et al. Ultra-long-term reliable encapsulation using an atomic layer deposited $HfO_2/Al_2O_3/HfO_2$ triple-interlayer for biomedical implants. *Coatings* **9**, 579 (2019).
98. Wu, H. C. et al. Highly stretchable polymer semiconductor thin films with multi-modal energy dissipation and high relative stretchability. *Nat. Commun.* **14**, 8382 (2023).
99. Choi, Y. S. et al. Biodegradable polyanhydrides as encapsulation layers for transient electronics. *Adv. Funct. Mater.* **30**, 2000941 (2020).
100. Roberts, A. P. et al. Gas permeation in silicon-oxide/polymer (SiOx/PET) barrier films: role of the oxide lattice, nano-defects and macro-defects. *J. Membr. Sci.* **208**, 75–88 (2002).
101. Kim, L. H. et al. Optimization of Al2O3/TiO2 nanolaminate thin films prepared with different oxide ratios, for use in organic light-emitting diode encapsulation, via plasma-enhanced atomic layer deposition. *Phys. Chem. Chem. Phys.* **18**, 1042–1049 (2016).
102. Meyer, J. et al. Al_2O_3/ZrO_2 nanolaminates as ultrahigh gas-diffusion barriers—a strategy for reliable encapsulation of organic electronics. *Adv. Mater.* **21**, 1845–1849 (2009).
103. Kang, K. S., Jeong, S. Y., Jeong, E. G. & Choi, K. C. Reliable high temperature, high humidity flexible thin film encapsulation using Al_2O_3/MgO nanolaminates for flexible OLEDs. *Nano Res.* **13**, 2716–2725 (2020).
104. Kwon, J. H., Jeon, Y. & Choi, K. C. Robust transparent and conductive gas diffusion multibarrier based on Mg- and Al-doped ZnO as indium tin oxide-free electrodes for organic electronics. *ACS Appl. Mater. Interfaces* **10**, 32387–32396 (2018).
105. Kim, H., Kim, J. M., Lee, J. H. & Jang, J. G. Flexible encapsulation of organic light-emitting diode using the LiF/polymer/LiF buffer and metal foil. *Mol. Cryst. Liq. Cryst.* **601**, 190–196 (2014).
106. Dollinger, F., Nehm, F., Müller-Meskamp, L. & Leo, K. Laminated aluminum thin-films as low-cost opaque moisture ultra-barriers for flexible organic electronic devices. *Org. Electron.* **46**, 242–246 (2017).
107. Woo, J. H. et al. Highly elastic and corrosion-resistive metallic glass thin films for flexible encapsulation. *ACS Appl. Mater. Interfaces* **14**, 5578–5585 (2022).
108. Lee, S. et al. Study of mechanical degradation of freestanding ALD Al_2O_3 by a hygrothermal environment and a facile protective method for environmentally stable Al_2O_3: toward highly reliable wearable OLEDs. *Mater. Horiz.* **10**, 4488–4500 (2023).
109. Forte, M. A., Silva, R. M., Tavares, C. J. & Silva, R. F. E. Is poly(methyl methacrylate) (PMMA) a suitable substrate for ALD?: a review. *Polymers* **13**, 1346 (2021).
110. Maxwell, J. *Treatise on Electricity and Magnetism* (Clarendon Press, 1881).
111. Nielsen, L. E. Models for the permeability of filled polymer systems. *J. Macromol. Sci. Chem.,A.* **1**, 929–942 (1967).
112. Bharadwaj, R. K. Modeling the barrier properties of polymer-layered silicate nanocomposites. *Macromolecules* **34**, 9189–9192 (2001).
113. Mariani, P. et al. Low-temperature strain-free encapsulation for perovskite solar cells and modules passing multifaceted accelerated ageing tests. *Nat. Commun.* **15**, 4552 (2024).
114. Xia, R. et al. Hermetic stretchable seals enabled by a viscoplastic surface effect. *Nat. Mater.* **24**, 2011–2018 (2025).

115. Dickey, M. D. Stretchable and soft electronics using liquid metals. *Adv. Mater.* **29**, 1606425 (2017).
116. Ma, Z. et al. Permeable superelastic liquid-metal fibre mat enables biocompatible and monolithic stretchable electronics. *Nat. Mater.* **20**, 859–868 (2021).
117. Shen, Q. et al. Liquid metal-based soft, hermetic, and wireless-communicable seals for stretchable systems. *Science* **379**, 488–493 (2023).
118. Kan, R. et al. Liquid metal-elastomer seals for stretchable organic electrolyte-based lithium-ion batteries. *Adv. Funct. Mater.* **34**, 2309861 (2024).
119. Sun, H. et al. Liquid-based encapsulation for implantable bioelectronics across broad pH environments. *Nat. Commun.* **16**, 1019 (2025).
120. Sun, H. et al. Bioinspired oil-infused slippery surfaces with water and ion barrier properties. *ACS Appl. Mater. Interfaces* **13**, 33464–33476 (2021).
121. Choi, D.-w, Kim, S.-J., Lee, J. H., Chung, K.-B. & Park, J.-S. A study of thin film encapsulation on polymer substrate using low temperature hybrid ZnO/Al_2O_3 layers atomic layer deposition. *Curr. Appl. Phys.* **12**, S19–S23 (2012).
122. Wang, B., Bao, S., Vinnikova, S., Ghanta, P. & Wang, S. Buckling analysis in stretchable electronics. *NPJ Flex. Electron.* **1**, 5 (2017).
123. Peng, Y. et al. Improved mechanical properties of Al_2O_3/acrylic laminates for flexible thin film encapsulation by introducing wavy interfaces. *Org. Electron.* **117**, 106791 (2023).
124. Choi, D. K. et al. Highly efficient, heat dissipating, stretchable organic light-emitting diodes based on a MoO(3)/Au/MoO(3) electrode with encapsulation. *Nat. Commun.* **12**, 2864 (2021).
125. Jin, P. et al. Fluid microchannel encapsulation to improve the stretchability of flexible electronics. *Adv. Mater. Technol.* **7**, 2101126 (2021).
126. Shin, Y. J. et al. Stretchable fabric organic light-emitting diodes based on transferable laser pattern for wearable photodiagnostic applications. *Adv. Fiber Mater.* **7**, 908–925 (2025).
127. Kim, N., Kim, J., Seo, J., Hong, C. & Lee, J. Stretchable inorganic LED displays with double-layer modular design for high fill factor. *ACS Appl. Mater. Interfaces* **14**, 4344–4351 (2022).
128. Moon, M.-W. & Vaziri, A. Surface modification of polymers using a multi-step plasma treatment. *Scr. Mater.* **60**, 44–47 (2009).
129. Chen, S. H., Chan, K. C., Yue, T. M. & Wu, F. F. Highly stretchable kirigami metallic glass structures with ultra-small strain energy loss. *Scr. Mater.* **142**, 83–87 (2018).
130. Wang, K.-N. et al. The applications of flexible electronics in dental, oral, and craniofacial medicine. *NPJ Flex. Electron.* **8**, 33 (2024).
131. Chen, B. et al. Flexible piezoelectrics: integration of sensing, actuating and energy harvesting. *NPJ Flex. Electron.* **9**, 58 (2025).
132. Verduci, R. et al. Solar energy in space applications: review and technology perspectives. *Adv. Energy Mater.* **12**, 2200125 (2022).
133. Tu, Y. et al. Perovskite solar cells for space applications: progress and challenges. *Adv. Mater.* **33**, e2006545 (2021).
134. Li, T. et al. A skin-conformal and breathable humidity sensor for emotional mode recognition and non-contact human-machine interface. *NPJ Flex. Electron.* **8**, 3 (2024).
135. Sutherland, L. J., Weerasinghe, H. C. & Simon, G. P. A review on emerging barrier materials and encapsulation strategies for flexible perovskite and organic photovoltaics. *Adv. Energy Mater.* **11**, 2101383 (2021).
136. Lu, Q. et al. A review on encapsulation technology from organic light emitting diodes to organic and perovskite solar cells. *Adv. Funct. Mater.* **31**, 2100151 (2021).

Acknowledgements

This work was supported by the National Research Foundation of Korea (NRF) grant by the Korea government (MSIT) (RS-2025-25441247 and RS-2025-02305569) and by the InnoCORE program of the Ministry of Science and ICT (1.250021.01). This study contains the results obtained by using the equipment of UNIST Office of Research Facilities and Training (ResFacT).

Author contributions

Author contributions are as follows: Investigation and writing—original draft: H.Y., S.-H.L., J.-Y.K., S.-M.K., H.-Y.J., J.-H.J., Y.K., Y.S., D.-H.K., J.J., S.H., S.-J.K., and J.-Y.K. Figures: H.Y., S.-H.L., J.-Y.K., S.-M.K., H.-Y.J., J.-H.J., G.-S.H., and J.-W.G. Table: S.-H.L. Writing—review & editing: H.Y., S.-H.L., H.-H.C., S.-K.K. and J.-Y.K. Conceptualization and supervision: J.-Y.K. All authors discussed and commented on the manuscript.

Competing interests

The authors declare no competing interests.

Additional information

Correspondence and requests for materials should be addressed to Ju-Young Kim.